

Ocean Wind Wave Climate Responses to Wintertime North Atlantic Atmospheric Transient Eddies and Low-Frequency Flow

M. Y. MARKINA

Shirshov Institute of Oceanology, Russian Academy of Sciences, and Lomonosov Moscow State University, Moscow, Russian Federation

J. H. P. STUDHOLME

Shirshov Institute of Oceanology, Russian Academy of Sciences, Moscow, Russian Federation

S. K. GULEV

Shirshov Institute of Oceanology, Russian Academy of Sciences, and Lomonosov Moscow State University, Moscow, Russian Federation

(Manuscript received 7 September 2018, in final form 28 November 2018)


ABSTRACT

Atmospheric transient eddies and low-frequency flow contributions to the ocean surface wave climate in the North Atlantic during boreal winter are investigated (1980–2016). We conduct a set of numerical simulations with a spectral wave model (WAVEWATCH III) forced by decomposed wind fields derived from the ERA-Interim reanalysis (0.7° horizontal resolution). Synoptic-scale processes (2–10-day bandpassed winds) are found to have the largest impact on the formation of wind waves in the western midlatitudes of the North Atlantic along the North American and western Greenland coasts. The eastern North Atlantic is found to be influenced by the combination of low-frequency forcing (>10-day bandpassed winds) and synoptic processes, contributing up to 60% and 30% of the mean wave heights, respectively. Midlatitude storm track variability is found to have a direct relationship with wave height variability along the eastern and western margins of the North Atlantic, implying an association between cyclogenesis over the North American eastern seaboard and wave height anomalies in the eastern North Atlantic. A change in wave height regimes defined using canonical correlation analysis is reflected in changes to their wave height distribution shapes. The results highlight the important role of transient eddies for the ocean surface wave climatology in the midlatitudes of the eastern North Atlantic both locally and through association with cyclone formation in the western part of the basin. These conclusions are presented and discussed particularly within the context of long-term storm track shifts projected as a possible response to climate warming over the coming century.

1. Introduction

Ocean surface wind waves, also known as surface gravity waves, influence upper-ocean turbulence and mixing (Babanin 2006; Babanin et al. 2009), heat and momentum air–sea fluxes (Komen et al. 1994; Veron et al. 2008; Sullivan and McWilliams 2002; Högström et al. 2009), the production of atmospheric aerosols via bubbles and sea spray (de Leeuw et al. 2011; Babanin

2011; Andreas et al. 2015), sea ice formation and breaking (Thomson and Rogers 2014; Kohout et al. 2014), and ice shelf disintegration (Massom et al. 2018). Due to these numerous interactions with the atmospheric boundary layer, cryosphere, and upper-ocean dynamics, ocean surface wave processes are becoming increasingly recognized as fundamental to climate over a range of spatial and temporal scales (e.g., Cavaleri et al. 2012; Fan and Griffies 2014; Babanin et al. 2012; D’Asaro 2014; Qiao et al. 2016; Walsh et al. 2017; Fan et al. 2009; Aijaz et al. 2017; Stoney et al. 2018). In practical terms, information about extreme waves is also critical for planning marine operations and the design of offshore marine infrastructure (Cardone et al. 2015). Ocean surface waves bear

 Denotes content that is immediately available upon publication as open access.

Corresponding author: Margarita Markina, markina@sail.msk.ru

DOI: 10.1175/JCLI-D-18-0595.1

© 2019 American Meteorological Society. For information regarding reuse of this content and general copyright information, consult the [AMS Copyright Policy](#) (www.ametsoc.org/PUBSReuseLicenses).

the signature of synoptic-scale atmospheric dynamics (e.g., Gulev and Grigorjeva 2006; Semedo et al. 2015; Martínez-Asensio et al. 2016) and can transmit it over large spatial scales (Ardhuin et al. 2009; Delpy et al. 2010; Snodgrass et al. 1966). In this respect, wind waves are an important indicator of climate variability and the intensity of synoptic and mesoscale atmospheric processes.

This is particularly true in the North Atlantic, which is characterized by high-magnitude and strong variability in wind wave activity, especially throughout boreal winter (Gulev et al. 2003; Semedo et al. 2008; Hanley et al. 2010; Semedo et al. 2011). This is the direct result of midlatitude baroclinicity in general and, more specifically, the vigorous flow that comprises the regional atmospheric storm track and eddy-driven jet. Many authors have demonstrated a statistical association between the interannual variability in wind wave climate and time-averaged atmospheric characteristics, such as interannual fluctuations in the large-scale meridional pressure gradient referred to as the North Atlantic Oscillation (NAO; Bacon and Carter 1993; Carretero et al. 1998; Gulev and Hasse 1999; Wang and Swail 2001; Woolf et al. 2002; Wang et al. 2004; Camus et al. 2014). There is a great deal of discussion regarding storm track variability and so-called poleward deflection (e.g., Tamarin-Brodsky and Kaspi 2017; Booth et al. 2017), which has been found in some but not all reanalyses (Tilinina et al. 2013) as well as some model simulations corresponding to warming climate scenarios (Pinto et al. 2007; Fan et al. 2013; Woollings et al. 2012). Uncertainties in local storm track and eddy-driven jet changes propagate into projections of wave climate and limit our ability to have confidence in these diverse projections (Hemler et al. 2013; Fan et al. 2014; Khon et al. 2014).

Differences in wave climate in the tropics and middle and high latitudes are associated with the differences in dominant atmospheric circulations. In the tropics, summer wave heights are strongly impacted by changes in the intensity and frequency of tropical cyclones (e.g., Teague et al. 2007; Phibbs and Toumi 2014). These cyclones are generally expected to become relatively sparser but more intense and a change in their zonal and meridional distributions over the coming century is also expected to occur (e.g., Bender et al. 2010; Knutson et al. 2013; Studholme and Gulev 2018). At subpolar and polar latitudes, both winter and summer increases in seasonal mean and maximum waves have been identified over the last 36 years (Waseda et al. 2018) and are projected to continue into the coming century (Casas-Prat et al. 2018). These regime changes are expected to result from a set of complex wave responses to both wind and sea ice forcings acting simultaneously (Khon et al. 2014).

In the midlatitudes, wind wave climate is associated with storm track activity (Lozano and Swail 2002). A poleward shift in the midlatitude storm track is one of the most widely discussed features in the observational records (Bender et al. 2012) and numerical model simulations of future climate warming (Woollings et al. 2012; Bengtsson et al. 2006; Mbengue and Schneider 2017). This can be mostly understood as a response to an alteration of the tropospheric meridional temperature gradient and associated vertical shear. In addition, a poleward shift of the jet stream is observed (Woollings and Blackburn 2012), as well as a strengthening and poleward (and upward) shift in transient kinetic energy and momentum flux (Lorenz and DeWeaver 2007). Yin (2005) found that midlatitude westerlies also demonstrated a poleward shift. Ensemble mean model projections demonstrate evidence for increasing storm track activity in the eastern North Atlantic, amounting to a 5%–8% increase in baroclinic wave activity by the end of the twenty-first century (Ulbrich et al. 2008, 2013). However, a considerable spread among models is found (Harvey et al. 2012; Zappa et al. 2013a).

Wind wave climate variability in the midlatitudes is strongly associated with extratropical cyclonic activity via changes in wind speeds. In turn, atmospheric transient eddies may demonstrate different patterns of interannual variability from the mean winds and pressure gradients, especially locally (e.g., Gulev et al. 2002). The response of the wind wave climate to atmospheric forcing is quite complex since waves in the open ocean are a composition of locally generated wind sea and remotely generated swell (Young et al. 2011). Thus, wind wave climate reflects local trends in wind speed and the frequency and intensity of atmospheric processes integrated over larger scales. Quantifying the responses of wind wave climate to the varying impacts of different spatial and temporal scales of atmospheric motions presents a considerable challenge. In this respect, numerical wind wave modeling represents an effective tool for the simulation of wave characteristics as a function of varying atmospheric forcings.

Here, our aim is to derive insights into how variability in atmospheric dynamical processes of different length scales affects wave climate. As a case study, we conduct and analyze a suite of numerical experiments during boreal winter in the North Atlantic. Ultimately, improved understanding here may help to constrain and better understand uncertainties in wave climate projections. This paper is organized as follows: Section 2 gives model details, datasets, and the analysis methodology. Section 3 examines the responses of the simulated wind waves to decomposed atmospheric forcing. Section 4 discusses the

link between wave climate and atmospheric interannual variability at different scales. Section 5 provides a brief discussion of the potential uncertainties as well as avenues for future work. The conclusions are presented in section 6.

2. Numerical simulations

a. Wave model and experiment design

The simulations in this study were conducted with version 5.16 of the third-generation spectral wave model WAVEWATCH III (WW3 herein; WAVEWATCH III Development Group 2016) for the North Atlantic from 0° to 80°N and 90°W to 15°E. For this domain, the influence of swell originating from south of the equator is considered to be negligible and is thus ignored (e.g., Alves 2006). We use the ST4 parameterization for wave energy input and dissipation (Ardhuin et al. 2010) and the Discrete Interaction Approximation (DIA) scheme for nonlinear wave interactions (Hasselmann and Hasselmann 1985). The model integration time step is 15 min. The simulations were performed for the boreal winter season [December–February (DJF)] over the period 1980–2016. Individual model runs are initiated two weeks in advance (i.e., mid-November) to account for the model spinup. This initialization period is discarded from further calculations. The model settings described above have been used in a number of wave climate studies (e.g., Chawla et al. 2013; Rascle and Ardhuin 2013; Markina et al. 2018).

Each seasonal experiment was run at 0.7° spatial resolution and forced by 10-m winds from the European Centre for Medium-Range Weather Forecasts (ECMWF) interim reanalysis (ERA-Interim) dataset (Dee et al. 2011). ERA-Interim is the demonstrably optimal reanalysis dataset to use for interannual studies of wave climate due to its relative consistency over the record period in comparison to alternative products (Stopa and Cheung 2014). The ice source term package (IC0; Tolman 2003) used in our WW3 configuration assumes the exponential attenuation of waves in partially sea ice-covered regions given by 12-hourly sea ice concentrations from the ERA-Interim reanalysis. Grid points are defined as partially covered when sea ice concentrations are between 25% and 75%. Grid points with sea ice concentrations below 25% are treated as open water, while those above 75% are assumed to have zero wave energy, and the boundary conditions along the ice edges are considered the same as those for shore lines.

Throughout this manuscript, we use the notation *FULL* to refer to the results of the experiment forced by the original ERA-Interim winds. The *FULL* simulation

serves as the reference model run. In three further experiments, the wind forcing was decomposed into three components corresponding to short-term subsynoptic variability (0–2 days), hereafter referred to as *SUBS*; synoptic-scale variability (defined here as 2–10 days; e.g., Hoskins and Hodges 2002), hereafter referred to as *SYNO*; and low-frequency variability (more than 10 days), hereafter referred to as *LF*. A similar decomposition was previously used by Ayrault et al. (1995), Gulev et al. (2002), and Foussard et al. (2019). The wind field decomposition was performed using a bandpass Lanczos filter (Lanczos 1956; Duchon 1979), which was effectively used earlier by Gulev et al. (2002).

b. Diagnostics

We concentrate on significant wave height H_s and mean wave direction θ , which are derived from the spectral model solution at grid points that are free from sea ice for the entire period covered by the model integrations. In the analysis of covariability between wave climate and atmospheric variability (section 4), we discuss mean and extreme characteristics (95th percentile). The maximum values of H_s discussed in section 3 are used as proxies for the upper bound of the simulated wave heights (e.g., Caires and Sterl 2005; Janssen 2015), which are defined as seasonal-maximum values averaged over the period 1980–2016 (DJF).

As an Eulerian measure of the intensity of atmospheric dynamical processes over a range of scales we use vertically integrated eddy kinetic energy (EKE) (Lorenz 1955; Orlandi and Katzfey 1991) computed from <2, 2–10, and >10 day bandpass filtered 6-hourly wind fields (Blackmon 1976; Blackmon et al. 1977; Hoskins and Hodges 2002; Schneider et al. 2015; Woollings et al. 2016). The expression for EKE is given by

$$\text{EKE} = \int_{800}^{200} \left(\overline{u'^2} + \overline{v'^2} \right) dp / 2g, \quad (1)$$

where u' and v' represent the bandpass filtered zonal and meridional components of wind speed, respectively; p represents pressure (the vertical coordinate); and g represents acceleration due to gravity. We use bandpass filtering to isolate atmospheric transient eddies since there is a risk of inadvertently including stationary eddies in more rudimentary eddy identification schemes (e.g., Mbengue et al. 2018). The remaining <2-day and >10-day bandpassed flows act as high-frequency (i.e., subsynoptic processes) and low-frequency modes of atmospheric forcing. The integral is evaluated between 800 and 200 hPa to capture dynamical processes in the free troposphere (e.g., Mbengue et al. 2018). Since we are particularly interested in midlatitude baroclinicity, a collection of

potential metrics exist that could be used for this purpose. In particular, in addition to the vertically integrated EKE, near-surface eddy meridional heat fluxes ($v'\theta'$) and upper-tropospheric eddy momentum flux convergence ($-\nabla u'v'$) are both viable candidates as measures of the baroclinic eddy life cycle (e.g., Chang et al. 2002; Mbengue and Schneider 2013). Since we are interested in atmospheric dynamical processes more generally, EKE is the logical candidate for the present analysis.

Figure 1 shows climatological EKE for different bandpassed ranges computed according to Eq. (1) and the mean cyclone track density during the winter season (DJF) from 1980 to 2016 (Fig. 1b). The maximum values of EKE in the synoptic range ($\sim 5.2 \times 10^5 \text{ J m}^{-2}$) are located to the east of Newfoundland and are associated with the region of intensive cyclogenesis and development in the North Atlantic. The highest-frequency mode (i.e., *SUBS*) of EKE (Fig. 1a) demonstrates a spatial structure very similar to its synoptic-scale counterpart, although with half the magnitude. By the nature of the bandpass procedure, bundled in with true subsynoptic dynamical processes, *SUBS* filtering may also contain a small number of synoptic-scale processes, such as fast propagating cyclones (e.g., Rudeva and Gulev 2011). The low-frequency filtering of EKE (Fig. 1c) has the largest magnitudes (up to $\sim 30 \times 10^5 \text{ J m}^{-2}$) and this is an order of magnitude larger than EKE for the other components. The maximum values coincide at similar locations as in *SUBS* and *SYNOPT*, but *LF* also reveals an additional second maximum in the eastern subtropics. This EKE pattern (i.e., an Eulerian measure of the storm track) is highly consistent with the pattern for cyclone counts (i.e., a Lagrangian measure of storm track density) in the North Atlantic, which is also shown in Fig. 1b. Lagrangian statistics have been derived from ERA-Interim storm tracks provided by K. Hodges at the University of Reading, as used in Roberts et al. (2014), based on a methodology described in Hoskins and Hodges (2002) and Hodges (1995). These storm tracks exhibit high consistency with the cyclone track climatologies available from other numerical tracking algorithms applied to ERA-Interim (Neu et al. 2013; Rudeva and Gulev 2011; Tilinina et al. 2013). There is a strong correspondence between the Eulerian and Lagrangian characterizations of the storm track in this particular region that is critical for wave formation (Gulev and Grigorjeva 2006). The Lagrangian tracking algorithm also appears to pick up a second local maxima off the southeastern coast of Greenland, which is presumably either large polar lows (Stoll et al. 2018) or cyclones associated with the Greenland tip jets (Våge et al. 2009) that are not seen in the climatological EKE.

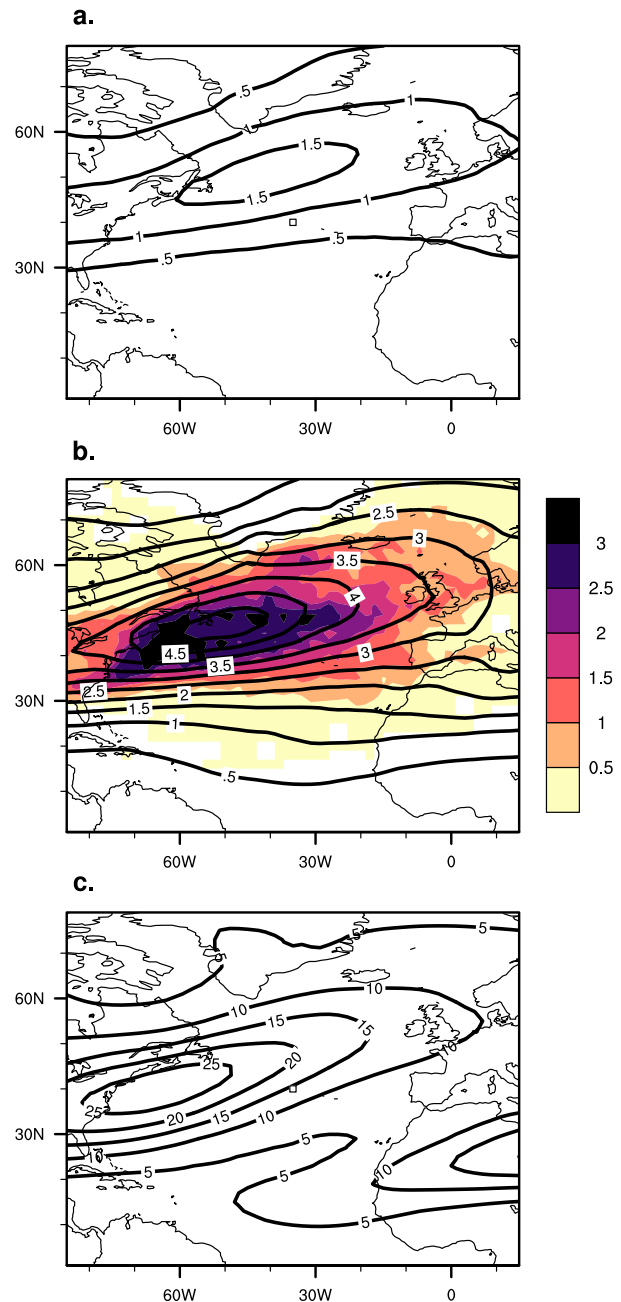


FIG. 1. Climatological seasonal-mean vertically integrated eddy kinetic energy (contours; $\times 10^5 \text{ J m}^{-2}$) bandpass-filtered for (a) < 2 days, (b) 2–10 days, and (c) > 10 days. Contour spacing is $5 \times 10^5 \text{ J m}^{-2}$. Cyclone track density per season (DJF) per 2° box in 1980–2016 is shown in shading in (b).

3. Wave climate responses to different scale atmospheric dynamical processes

a. Climatologies

The climatological seasonal-mean and seasonal-maximum distributions of wave heights and directions

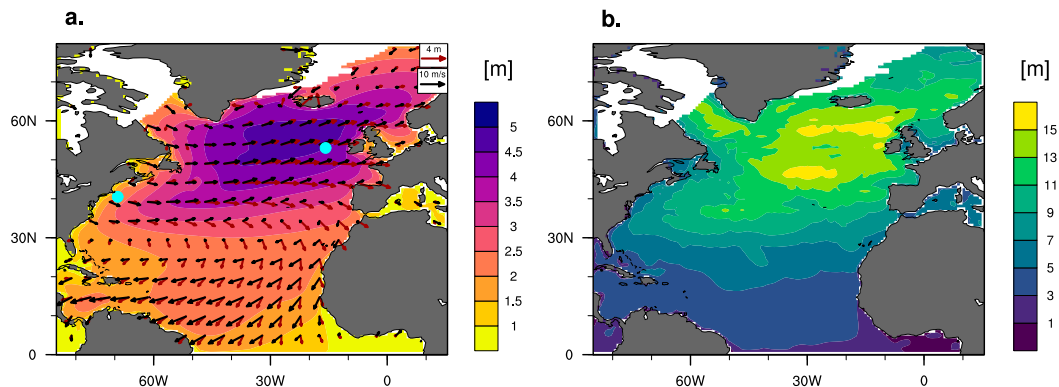


FIG. 2. Climatological (a) seasonal-mean and (b) seasonal-maximum H_s (shading) and mean wave and wind directions (red and black vectors, respectively) for DJF 1980–2016 (*FULL*). Colored dots correspond to buoy sites used in further analysis.

(DJF; 1980–2016) from the reference simulation (Fig. 2) show a maximum H_s of ~ 4.7 m in the northeastern sector of the North Atlantic, which is consistent with voluntary observing ship (VOS) observation climatologies (Gulev and Hasse 1998; Gulev et al. 2003), satellite data (Zieger et al. 2009; Young et al. 2017), and the ERA-Interim wave reanalysis (Dee et al. 2011). The pattern correlation with the ERA-Interim wave reanalysis is 0.97 for all winters (not shown), and the control experiment corresponds well with the U.S. National Data Buoy Center (NDBC) data in coastal areas (an example for 2010 is shown in Fig. A1 in appendix A). The seasonal-mean H_s is largest in an area displaced northeastward from the maximum storm track activity in the western North Atlantic (Fig. 2a). This pattern is generally consistent with the mean direction and spatial scales of swell propagation that contributes largely to the total significant wave heights in this region (Chen et al. 2002; Semedo et al. 2011). In areas with the most intensive wind wave formation, such as the western tropics and midlatitudes, the dominant wave direction (shown with red vectors) is more aligned with the mean wind direction (black vectors) than that over the rest of the domain.

The spatial structure of the seasonal-maximum H_s (Fig. 2b) reveals a pattern qualitatively similar to the one observed for the mean values (Fig. 2a), although with a noisier structure. There are several areas with maximum significant wave heights up to 15.9 m in the eastern midlatitudes, and there is a local peak in the Labrador Sea, with values up to 14 m. The observed spatial pattern reflects, to a certain degree, the influence of synoptic-scale atmospheric structures on the formation of wave height extremes.

Figure 3 shows model snapshots at 1200 UTC 30 December 2000 as obtained by the four aforementioned

experiments (i.e., *FULL*, *SUBS*, *SYNOP*, and *LF*). This figure demonstrates how the simulated wave structures are superimposed and related to a corresponding simulation with full forcing at any given time. The smoothest and most intense wind forcing field (*LF*) is reflected in large-scale wave patterns (Fig. 3c), while the synoptic-scale (*SYNOP*) and subsynoptic-scale (*SUBS*) processes in the atmosphere influence the surface ocean at shorter spatial scales (Figs. 3a,b). The reference simulation with full wind forcing (*FULL*; Fig. 3d) superimposes the combined effect of low- and high-frequency atmospheric forcing, as would be expected.

The climatological seasonal-mean H_s and θ distributions for all four simulations forced by the decomposed wind fields are presented in Fig. 4. The synoptic-scale processes, which are predominantly associated with cyclonic activity, are resolved into a spatial pattern with H_s magnitudes being maximal (up to 2 m) in the midlatitudes of the North Atlantic (Fig. 4b). Subsynoptic-scale processes, in general, have the largest impact in the same areas as those in the *SYNOP* experiment, while inducing waves that are twice as small (Fig. 4a). Low-frequency forcing dominates the wave distribution in the tropics (i.e., following the persistent, steady flow of the easterly trade winds; Fig. 4f), with H_s values up to 2.5 m in the western tropical Atlantic (Fig. 4c). In addition, the *LF* component has a large impact over the eastern North Atlantic in the midlatitudes in areas that have the largest wave heights in the reference model run (Fig. 2), with mean H_s up to 3 m. Therefore, the area of highest climatological H_s (Fig. 2), while mostly dominated by *LF*, is also influenced by *SUBS* and *SYNOP* processes, whose contributions are nonnegligible.

Both the *SUBS* and *SYNOP* simulations demonstrate an almost purely divergent structure in θ emanating out from where the storm track intensity is maximal, which

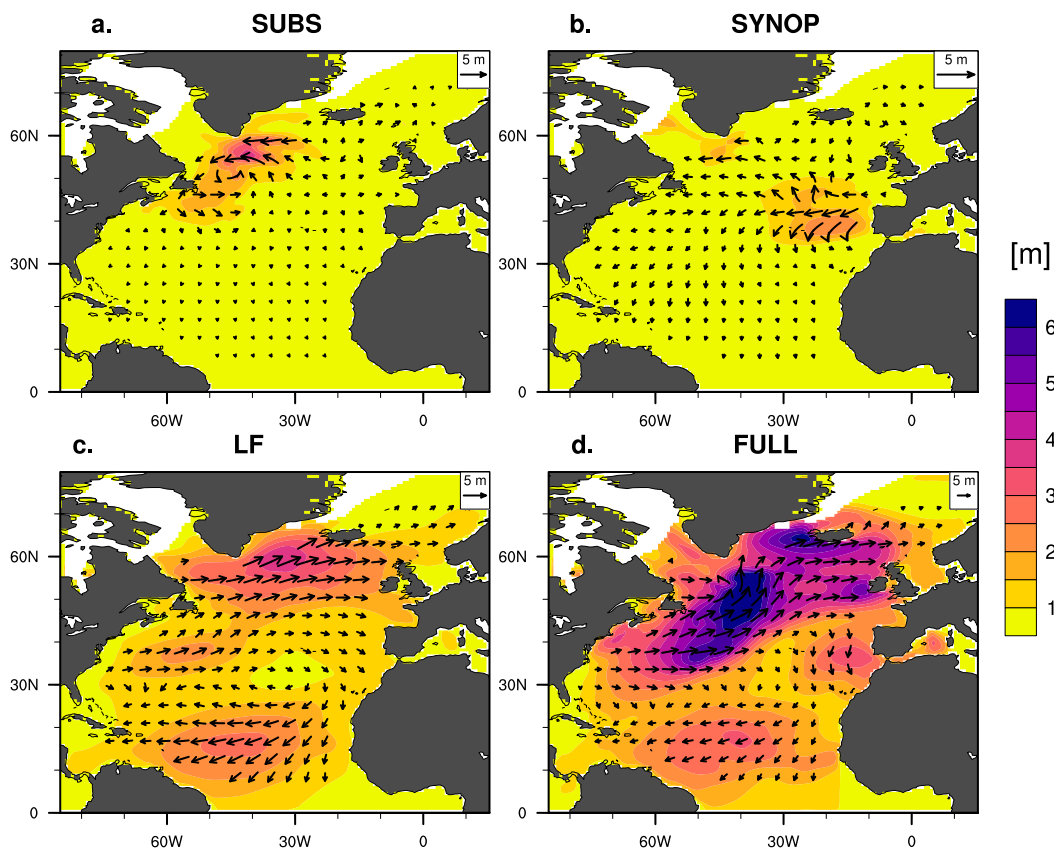


FIG. 3. Snapshots of H_s simulated by the decomposed wind fields (a) *SUBS*, (b) *SYNOP*, (c) *LF*, and (d) full forcing *FULL* at 1200 UTC 30 Dec 2000.

reflects the largely cyclonic origin of the momentum flux (i.e. surface stresses; Fig. 1 and Figs. 4a,b). The differences between these simulations and the control experiment (Figs. 4d,e) reveal strong negative deviations everywhere, with the largest differences along the eastern North Atlantic. These spatial characteristics reveal the association between waves driven by synoptic and subsynoptic processes and areas where the storm track is most active. These characteristics also emphasize the dominant role of low-frequency atmospheric flow in forcing wind waves in the eastern North Atlantic midlatitudes.

Figure 5 shows the responses of the wave height maxima to different atmospheric forcings in the same manner as Fig. 4 for does for the mean values. The patterns of maximum H_s in the *SUBS*, *SYNOP*, and *LF* experiments are noisier in comparison to those for the mean values (Fig. 4). The highest waves are identified in the Labrador Sea (in *SYNOP*) and the Irminger Sea along the eastern coast of Greenland (in *LF*). These signatures are not present in the distribution of the mean H_s (Fig. 4). The magnitudes of the maximum wave heights for all simulations with decomposed forcings are comparable (8, 9.6, and 8 m for *SUBS*,

SYNOP, and *LF*, respectively). Physically, this means that atmospheric motion across the entire range of temporal scales, from subsynoptic and synoptic transient eddies to lower-frequency oscillations, may have an influence of equal magnitude upon the ocean surface wave climate. The largest difference between the decomposed and reference simulations is observed in *SUBS* since this component initially has the lowest magnitudes of atmospheric forcing, which is reflected in the lowest values of the simulated H_s and amounts up to 16.5 m near the northern coast of the British Isles (Fig. 5d). For the *SYNOP* and *LF* experiments, the differences compared with *FULL* are up to 10 m (Figs. 5e,f) and are observed over the northeastern North Atlantic.

The similar magnitudes of the maximal H_s across the *SUBS*, *SYNOP*, and *LF* simulations imply that the respective probability density distributions for H_s have very different shapes. To illustrate these regional connections among different scales of atmospheric variability with wind wave heights, Fig. 6 shows histograms for H_s at the sites indicated by blue dots in Fig. 2a. Stronger midlatitude transient eddy activity

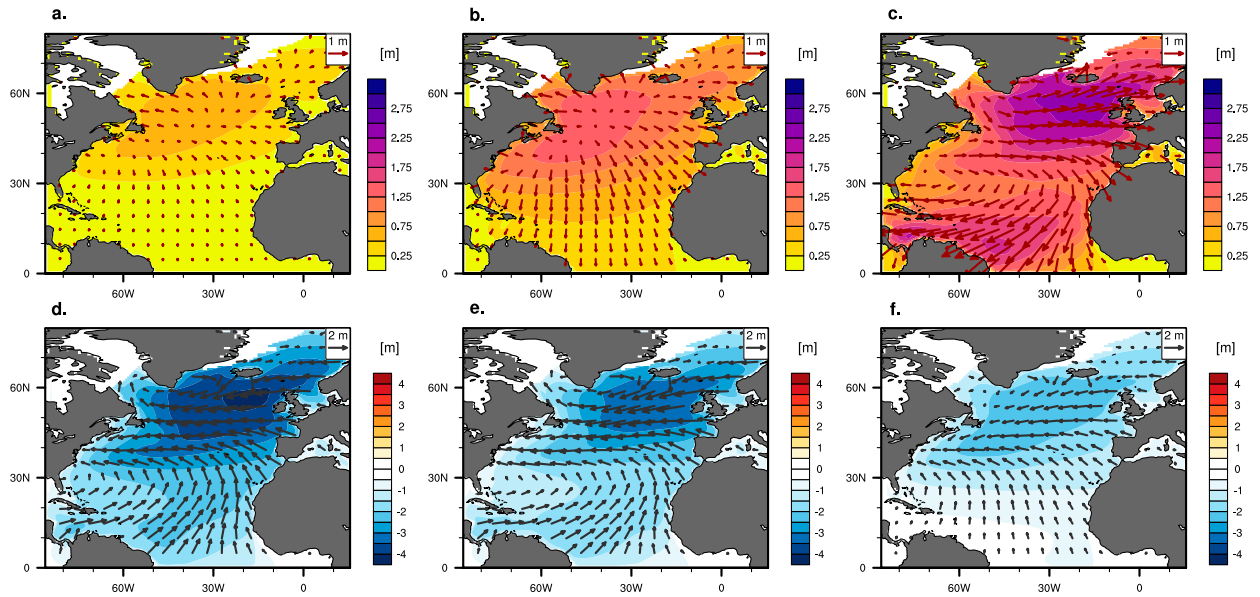


FIG. 4. Climatological seasonal-mean H_s (in DJF 1980–2016) and directions forced by decomposed wind fields: H_s and θ from (a) *SUBS*, (b) *SYNOPSIS*, and (c) *LF* simulations and their difference with full forcing simulations: (d) (*SUBS* – *FULL*), (e) (*SYNOPSIS* – *FULL*), and (f) (*LF* – *FULL*).

(i.e., an intensified storm track) leads to increased waves along the North American eastern seaboard, while it contributes less to waves along the European coast since they are highly affected by low-frequency atmospheric forcing (*LF*). Note also that transient eddies contribute mostly to low-magnitude waves

along the eastern margin of the basin up to 4 m near the coast of the British Isles (while the full range of H_s expands up to 10 m). Along the western margin, cyclonic activity contributes to very large values over the entire spectrum of the ocean surface wave distribution.

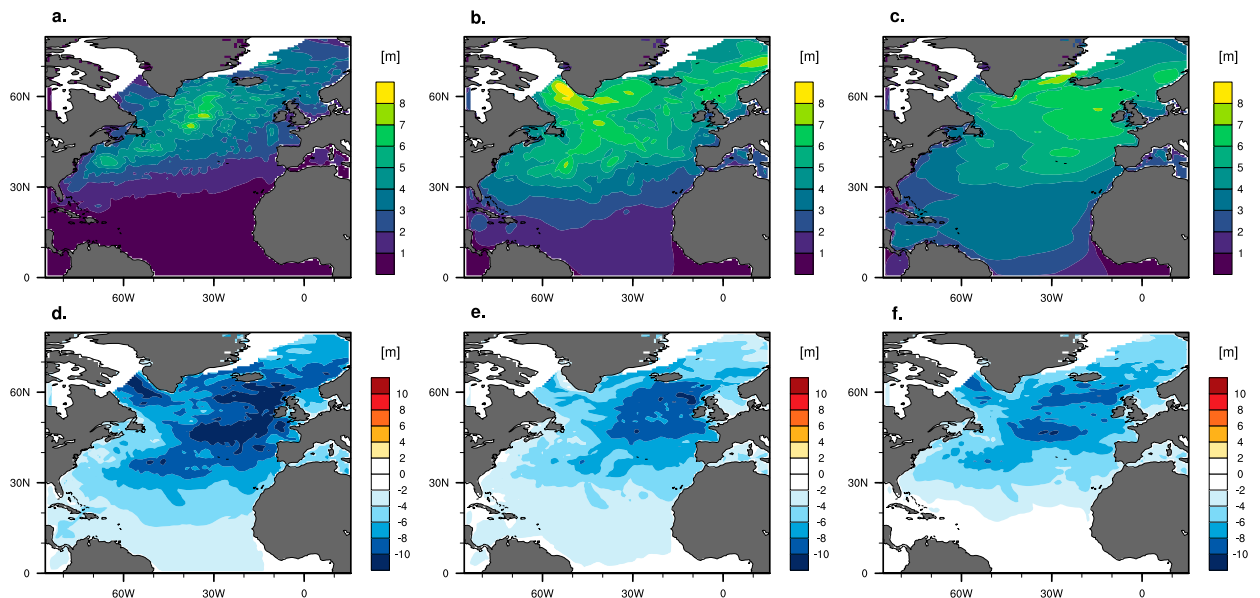


FIG. 5. Climatological seasonal-maximum H_s (DJF, 1980–2016) forced by decomposed wind fields: H_s from the (a) *SUBS*, (b) *SYNOPSIS*, and (c) *LF* simulations and their difference from full forcing simulations: (d) (*SUBS* – *FULL*), (e) (*SYNOPSIS* – *FULL*), and (f) (*LF* – *FULL*).

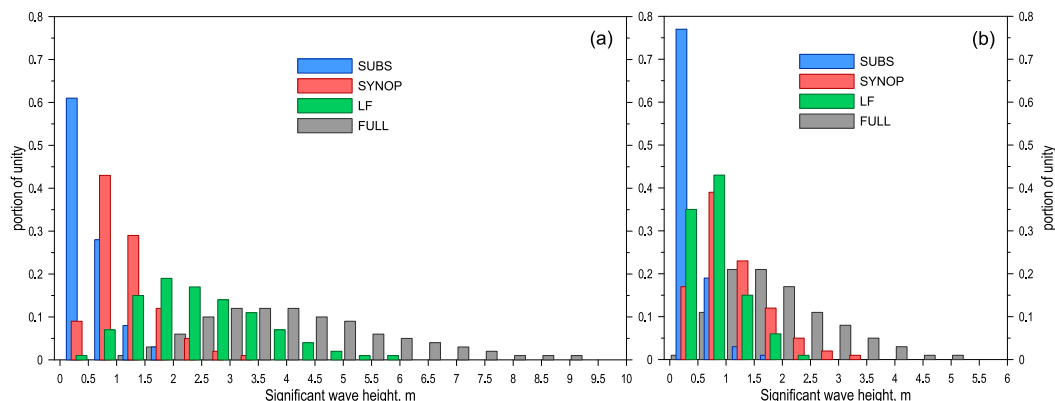


FIG. 6. Histograms of wave heights from *SUBS*, *SYNOPSIS*, *LF*, and *FULL* wave model simulations on the (a) eastern and (b) western margins of the North Atlantic sited in blue dots in Fig. 2a.

*b. Consideration of inherent nonlinearity:
Aggregated decomposed-forcing climates
compared to full-forced climate*

We note that the magnitudes of H_s in the *FULL* simulations are close but not exactly equal to the algebraic sum of the magnitudes of H_s in the simulations separately forced by the decomposed wind flow (i.e., $FULL \approx SUBS + SYNOPSIS + LF$). This result follows from the invocation of nonlinear processes in air–sea momentum fluxes, wave growth, and wave interactions. Moreover, the Lanczos filtering used for the wind forcing decomposition, while quite effective, may allow for the minor transfer of variance between the defined ranges (the so-called aliasing effect). Here, the aggregated sum of such aliasing in all filtered forcings corresponds to less than 1% of the total wind field over the majority of the domain. In the very deep tropics along the eastern boundaries, where climatological winds are $<3 \text{ m s}^{-1}$, such aliasing is maximal but even there this is less than 4% of the total forcing. Furthermore, these regions are confined and contribute very little to the overall wave climate. Therefore, the aliasing effect is negligible to the conclusions of this study.

The values for misalignment between *FULL* and $(SUBS + SYNOPSIS + LF)$ (Fig. 7) vary from -90% to 58% , with the average estimate being approximately -8.5% . The mean total difference between the algebraic sum of the simulations forced by decomposed wind fields and the magnitude of H_s in *FULL* is moderately negative, while there are high-magnitude positive values found along the North American coast. Atmospheric and surface wave processes responsible for this pattern over the western margin of the basin vary depending on latitude. In the tropics, this pattern most likely results from the relatively smooth and consistent trade winds retained in *LF*. In contrast, in the midlatitudes running up the eastern seaboard of the North American continent, this offshore

pattern is presumably dominated by transient eddies in the atmosphere in *SUBS* and *SYNOPSIS* because the influence of *LF* is relatively weak in this region, as discussed above (e.g., Fig. 6a and the corresponding discussion).

Moderately negative values of the differences are widespread around the eastern margin of the basin, which can presumably be explained by the wave growth resulting from the combination of numerous atmospheric processes operating simultaneously over a range of spatial and temporal scales (Fig. 3). The wave growth process is nonlinear (e.g., Miles 1957; Cavaleri and Malanotte-Rizzoli 1981) and, thus, an underestimation of the wave heights resulting from $(SUBS + SYNOPSIS + LF)$ relative to those revealed by the *FULL* experiment seems to be quite reasonable at the eastern midlatitudes. In the eastern tropics and equatorial region, the difference is strongly negative and, given generally low H_s magnitudes here (less than 1 m in the climatological seasonal mean;

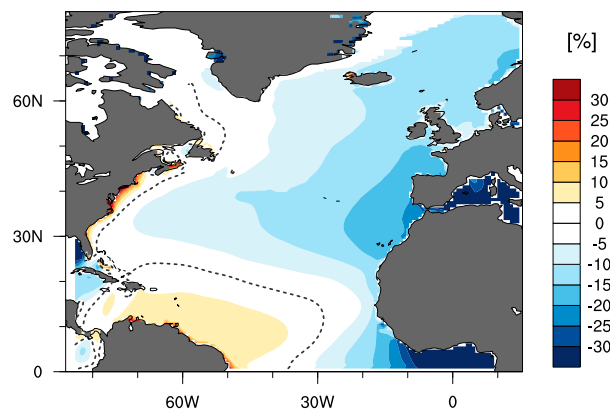


FIG. 7. Difference between sum of wave heights simulated by decomposed forcing and waves simulated by full forcing [i.e., $(SUBS + SYNOPSIS + LF) - (FULL)$]. The dashed line corresponds to zero.

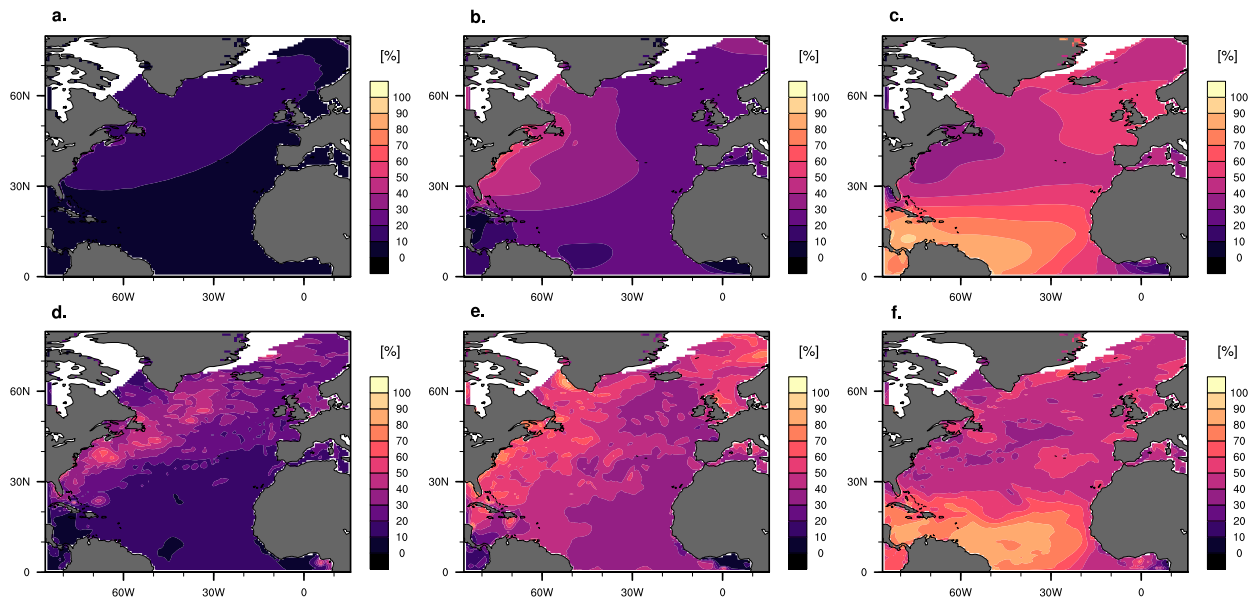


FIG. 8. Ratio between (top) mean and (bottom) maximum significant wave heights from simulations with decomposed forcing and reference simulations: (a),(d) $(SUBS)/(FULL) \times 100\%$, (b),(e) $(SYNOPSIS)/(FULL) \times 100\%$, and (c),(f) $(LF)/(FULL) \times 100\%$.

Fig. 2a), this difference is presumably associated with the persistent momentum flux in the *LF* simulations, which leads to the formation of higher waves relative to the *FULL* experiment. The same is true for the Gulf of Mexico.

To summarize the role of different forcing components in forming mean and maximum H_s , we consider the ratios between wave heights in the experiments with decomposed forcing and those in the reference experiment (*FULL*) for both the mean and maximum H_s (Fig. 8). For the maximum H_s , this ratio is further considered as a proxy for the upper bound of the observed contributions at different scales of the atmospheric dynamical processes to the wind wave climatology. Since the sum of the fractions is not equal to unity over most of the area, this diagnostic complements the analysis of the differences between the full and decomposed-forcing simulations presented above (Figs. 4d–f and 5d–f).

c. Relative contributions to actual wave climate provided by atmospheric dynamical processes of different scales

As mentioned above, the area with the maximum seasonal-mean H_s in the northeastern North Atlantic is influenced by all three components of wind forcing (up to 70%, 30%, and 20% in the *LF*, *SYNOPSIS*, and *SUBS* simulations, respectively). However, if we consider the seasonal-maximum values of H_s , *LF* accounts for up to 60%, with *SYNOPSIS* and *SUBS* contributing 50% and 40%, respectively. The area with the highest impact of

synoptic-scale atmospheric variability is located near the North American coast and in the Labrador Sea. The waves forced by synoptic-scale winds can be up to 80% of the mean and up to 90% of the maximum significant wave heights (Figs. 8b,e). At the same time, this area is affected by low-frequency atmospheric variability to a lesser extent (Figs. 8c,f): the *LF* simulation shows that waves have a general eastward direction (consistent with winds in *LF*), which thereby, does not provide favorable conditions for fetch along the North American coast. Subsynoptic-scale atmospheric processes do not significantly contribute to the mean wave characteristics (Fig. 8a), while they have a profound impact on the maximum waves (Fig. 8d) over the main North Atlantic storm track area (Fig. 1), particularly along the North American coast in the Gulf Stream region. The ratios for the wind fields are qualitatively similar (not shown), emphasizing the dominant role of low-frequency flow in the tropics and synoptic- and subsynoptic-scale processes in the midlatitudes.

To quantify the degree to which the different components contribute to the total variability in wave heights, we analyze the ratio between the standard deviations σ in each experiment relative to the control simulation. The largest values are observed in the *LF* simulation (Fig. 9c), where $\sigma(H_s)$ has approximately the same magnitude as that in the *FULL* simulation, which reflects the dominant role that *LF* forcing plays in wave formation in the tropics and semiencloded basins.

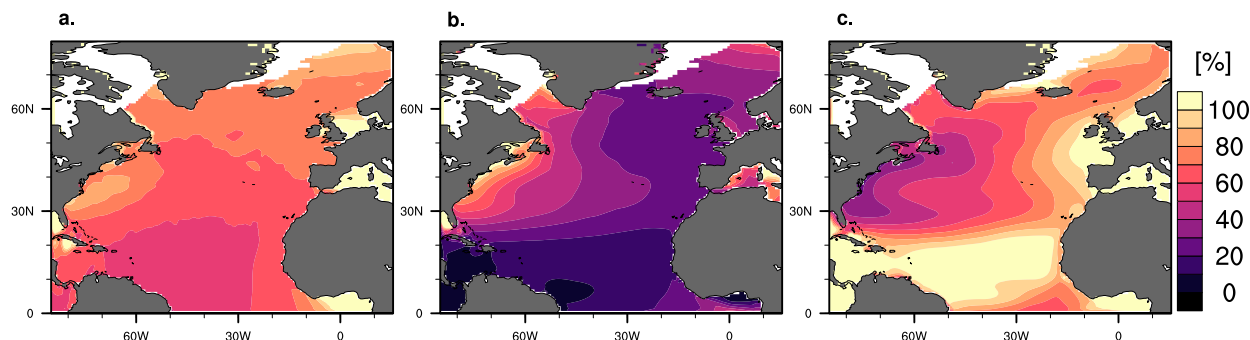


FIG. 9. Ratio between standard deviations of significant wave heights from simulations with decomposed forcing and reference simulations: (a) $[\sigma(SUBS)/\sigma(FULL)] \times 100$, (b) $[\sigma(SYNOP)/\sigma(FULL)] \times 100\%$, and (c) $[\sigma(LF)/\sigma(FULL)] \times 100\%$.

In the midlatitude open ocean the majority of the total variability in H_s is defined by a combination of synoptic-scale and low-frequency forcings, with differing impacts along the eastern and western margins. The variability observed in the LF simulations accounts for up to 100% of the total variability in H_s along the British Isles, while along the North American coast the major agent is the synoptic-scale forcing (up to 70% of the total variability; Fig. 9b). Wave heights from the $SUBS$ simulation demonstrate maximum variability compared to those in the control experiment in the semi-enclosed basins of the North Sea, the Mediterranean Sea, the Gulf of Mexico, and the Gulf of Guinea. The $SUBS$ simulation also produces a local maximum along the North American coast. Given that the upper bound of the contribution to the mean wave climate from the $SUBS$ scales is very low relative to that of $SYNOPSIS$ and LF (Figs. 8a–c) and that its contributions are homogenous in the North Atlantic (Fig. 9a), we neglect this dynamical length scale from further analysis and concentrate on the response of wind wave climate to synoptic and low-frequency modes of atmospheric forcing.

4. Linking wave climate and atmospheric interannual variability at different scales

To study the large-scale atmospheric flow patterns invoking specific wind wave responses, we use synoptic (2–10 day) and low-frequency (>10 day) filtered vertically integrated EKE (hereafter $EKE_{SYNOPSIS}$ and EKE_{LF} , respectively; Figs. 1b,c) as proxies for the intensity of atmospheric dynamical processes with the largest impacts on wave height dynamics in the North Atlantic. We explore the covariability of these characteristics with the mean H_s and θ from the simulations with full forcing (i.e., $EKE_{SYNOPSIS}$ vs H_s and θ ; EKE_{LF} vs H_s and θ). For this purpose, we applied canonical correlation analysis

(CCA; von Storch and Zwiers 1999) to the detrended seasonal (DJF) time series of EKE and wave characteristics. The first five empirical orthogonal functions (EOFs) were used for the CCA, and cumulatively they capture between 75.3% and 87.2% of the total variance for different variables. (Figure B1 shows the first two EOFs for $EKE_{SYNOPSIS}$ and EKE_{LF} with H_s and θ ; for details, see appendix B.) The CCA was applied to the following pairs of parameters: [$EKE_{SYNOPSIS}$ and H_s], [$EKE_{SYNOPSIS}$ and θ] (where the first and second CCA modes are presented in Figs. 10a and 10b, respectively), F10 [EKE_{LF} and H_s], and [EKE_{LF} and θ] (where the first and second CCA modes are presented in Figs. 10c and 10d, respectively). Since the CCA for EKE with both θ and H_s demonstrate very similar spatial patterns (not shown), we present only EKE from the CCA for [EKE and H_s] (Fig. 10).

The correlation coefficients between the first two modes of wave heights, θ and EKE (synoptic and low-frequency), are presented in Table 1. The correlation for the lead canonical pair is 0.90 for $EKE_{SYNOPSIS}$ (Fig. 10a) and 0.95 for EKE_{LF} (Fig. 10c). The obtained spatial patterns for $EKE_{SYNOPSIS}$ are consistent with the results of Lozano and Swail (2002). Interestingly, the absolute loadings of H_s are maximal at similar locations in the canonical patterns for both $EKE_{SYNOPSIS}$ and EKE_{LF} .

The first canonical pairs for both $EKE_{SYNOPSIS}$ and EKE_{LF} imply that the ocean surface wave height anomalies in the northeastern North Atlantic (i.e., the Norwegian and North Seas) and the wave height anomalies of opposite sign in the eastern North Atlantic are associated, which implies the meridional displacement of the storm track (Figs. 10a,c). The major difference in the spatial structures of these canonical patterns between synoptic and low-frequency variability is that the maximal loadings are strongly shifted across the basin eastward in $EKE_{SYNOPSIS}$ relative to EKE_{LF} . In

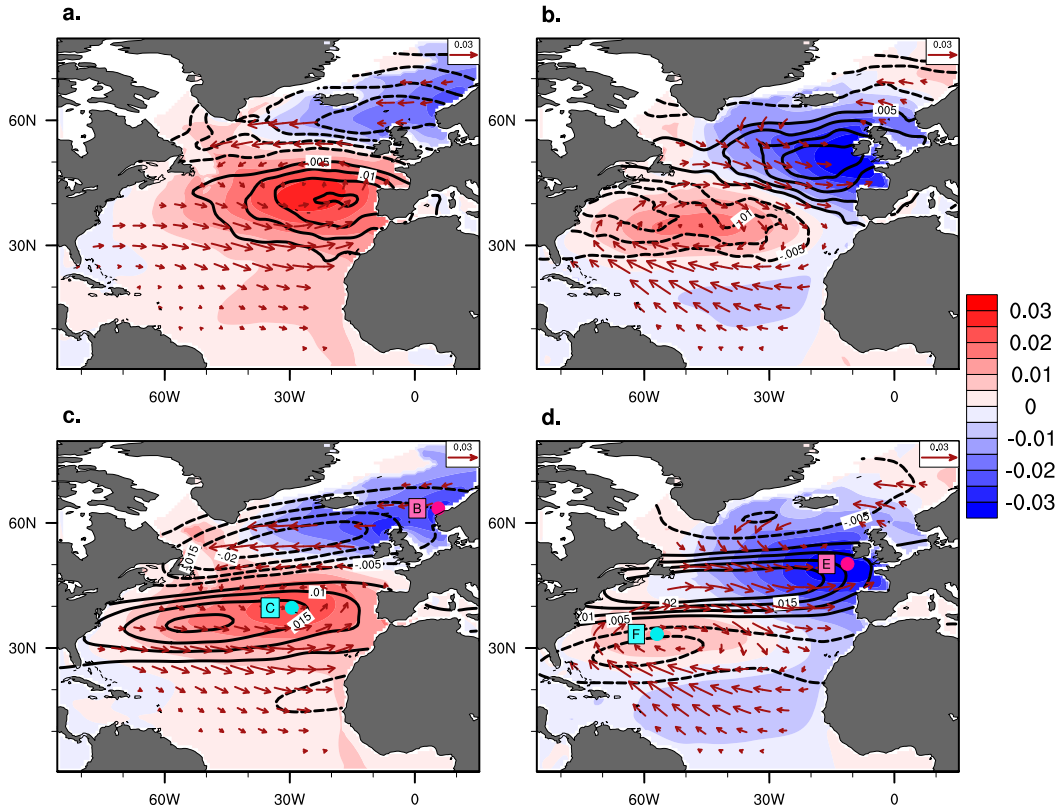


FIG. 10. The canonical spatial patterns of eddy kinetic energy, wave heights, and wave directions for the (a) first and (b) second canonical modes for $[EKE_{SYNOPSIS}$ and θ] and $[EKE_{SYNOPSIS}$ and H_s], and same for the (c) first and (d) second canonical modes for $[EKE_{LF}$ and θ] and $[EKE_{LF}$ and H_s]. Solid (dashed) lines indicate positive (negative) values of EKE canonical spatial patterns from CCA for $[EKE$ and $H_s]$. Vectors indicate canonical patterns for wave direction (θ). Red (blue) shading represents positive (negative) values of canonical patterns for wave heights (H_s). Dots are positioned at the locations of maximum (blue) and minimum (purple) values of H_s canonical pattern from the CCA for $[EKE_{LF}$ and $H_s]$. See text for more details regarding this plot.

general, the low-frequency flow demonstrates a much more zonal pattern than its synoptic counterpart. This result is also true for the second canonical pattern discussed below.

Unlike the similar first modes, the second canonical patterns for $EKE_{SYNOPSIS}$ and EKE_{LF} diverge from each other (Figs. 10b,d). The pattern for the synoptic atmospheric flow (Fig. 10b) is presumably associated with the storm track intensity, which indicates areas with positive $EKE_{SYNOPSIS}$ loading in the storm track region in the eastern part of the North Atlantic associated with negative H_s loading in the same region. The region of negative $EKE_{SYNOPSIS}$ anomalies near the North American coast is characterized by weaker loading by nearly an order of magnitude less than the aforementioned region of positive anomalies of $EKE_{SYNOPSIS}$ and is associated with wave height tendencies of the opposite sign. Positive wave anomalies in the western and central North Atlantic (south of Iceland) are closely associated with cyclone formation on the eastern margin of the

basin. Therefore, storm track activity in the western North Atlantic is profoundly connected to wind wave anomalies in the eastern North Atlantic.

The second canonical pattern of EKE_{LF} (Figs. 10d) indicates the strengthening of the zonal flow, which is reflected in the lower wave heights at eastern North Atlantic midlatitudes. In this way, lower wave heights at North Atlantic eastern midlatitudes can be considered either as a result of suppressed storm track activity (Fig. 10b) or a more intensive zonal flow in low-frequency

TABLE 1. Canonical correlation coefficients for the first two canonical pairs of wave heights and wave direction and synoptic and low-frequency modes of EKE.

| Canonical correlation | 1 | 2 |
|-------------------------------|------|------|
| EKE_{LF} and H_s | 0.95 | 0.86 |
| $EKE_{SYNOPSIS}$ and H_s | 0.90 | 0.75 |
| EKE_{LF} and θ | 0.96 | 0.95 |
| $EKE_{SYNOPSIS}$ and θ | 0.85 | 0.77 |

mode (Fig. 10d). The CCA for the 95th percentile of H_s (not shown) reveals a very similar spatial pattern to that observed for the mean values; hence, the above discussion is also applicable to extreme waves.

The patterns for the mean wave direction (θ) demonstrate a strong association with those observed for transient eddies and low-frequency flows (Fig. 10, shown in vectors). Larger values of EKE are associated with eastward wave propagation, whereas lower EKE values are associated with westward wave propagation. Interestingly, the pattern for wave direction is much more consistent with atmospheric variability, while wave heights demonstrate the eastward displacement of maximum loadings relative to EKE.

Finally, to examine the specific responses of wave heights in areas with the largest association with the synoptic and low-frequency bands of the storm track, we discuss the normalized occurrence anomalies of H_s . Figures 11b, 11c, 11e, and 11f correspond to 2° boxes, centered at sites indicated by purple and blue dots in Figs. 10c and 10d, respectively (annotated with letters corresponding to the subplots in Fig. 11). These sites are objectively identified as the locations where the CCA pattern for H_s is minimal (Figs. 11b,e) and maximal (Figs. 11c,f) in the first (Figs. 11b,c) and second (Figs. 11e,f) canonical modes, respectively. To visualize changes to the wave distribution depending on the state [i.e., value of the principal component (PC)] of the particular mode of variability (i.e., the CCA mode), we sort years as a function of their rank in the first and second PC time series from the H_s EOFs. The values of the PCs themselves are shown in Figs. 11a and 11d.

During the years with the lowest values of the first PC for H_s (i.e., 2010, 2001, 1996, 2013, 1982, and 2011), an increase in the occurrence of high waves is observed in the eastern part of the North Atlantic (Fig. 11c). Concurrently, a decrease in the occurrence of high waves is observed in the northeastern North Atlantic (Fig. 11b). The opposite pattern is observed during years with the highest values of the first PC (i.e., 1993, 1989, 1981, 2015, and 2012) in the northeastern part of the North Atlantic (Fig. 11b), where waves become higher in magnitude. Correspondingly, in the eastern North Atlantic (Fig. 11c), a negative anomaly in the number of high waves is observed.

For PC2, the pattern is quite noisy for the central North Atlantic (Fig. 11f), whereas in the northeastern North Atlantic (Fig. 11e) the pattern is close to that observed for PC1 (Fig. 11b). During years with the highest values of PC2 (i.e., 2014, 1990, 1994, 1995, and 2016), higher than normal waves are observed, whereas when moving toward the lowest values of PC2 we see a clear change in the wave height distribution toward lower values.

When considering extreme waves, changes in the 95th percentile of H_s are essentially consistent with the changes in wave distribution, as observed in the occurrence anomalies (Figs. 11b,c,e,f). The changes are subtler in the 95th percentile values, which change by only a few meters over the entire range of the PCs. Meanwhile, the maximum wave heights are heavily dependent on the sampling variability; therefore, they may not necessarily correspond to changes in the wave distribution. For example, this conclusion is true for 1990 (Fig. 11b), 1998 (Fig. 11c), and 2008 (Fig. 11e).

5. Discussion

Considering potential uncertainties in our results, it should be noted that all potential errors and misrepresentations inherent in surface winds are transmitted into wave models (Cavaleri 2009) because wind-driven momentum flux to the surface ocean is the only energetic source for wind wave growth. As such, important issues exist related to deriving a vertical wind profile in the atmospheric surface layer. These profiles are typically derived from Monin–Obukhov similarity theory (Obukhov 1946; Monin and Obukhov 1954), which is semiempirical and can be implemented in various flavors through the choice of stability classification and similarity functions. Small but nonnegligible diversity among such interpretations exists in models and reanalysis products (Jiménez et al. 2012).

Uncertainties in reanalysis surface winds may also include the impacts of inhomogeneities in data assimilation. An additional source of uncertainty is associated with the interpolation of atmospheric forcing characteristics between the model time steps, which is particularly relevant in the highly turbulent atmospheric boundary layer. In these experiments, atmospheric surface winds are linearly interpolated from 6-hourly ERA-Interim winds to the integration time step of the spectral wave model (15 min in this study). In this way, higher-resolution atmospheric forcing can provide a more reliable forcing for wave models because any local boundary layer particularities, as well as atmospheric transient eddies, can significantly alter in structure and location over the course of 6 h (e.g., Held and Hoskins 1985).

Additional nuances arise from the nonconstant nature of the drag coefficient C_D . In the model, C_D differences due to temperature are neglected, and only variations with wind velocity are used for its determination. We estimate that the effective (i.e., time-mean and domain-mean) wind speed in *FULL* is 6.9 m s^{-1} , while the analogous values in the filtered forcings are 1.6, 3.0, and 5.1 m s^{-1} for *SUBS*, *SYNOP*,

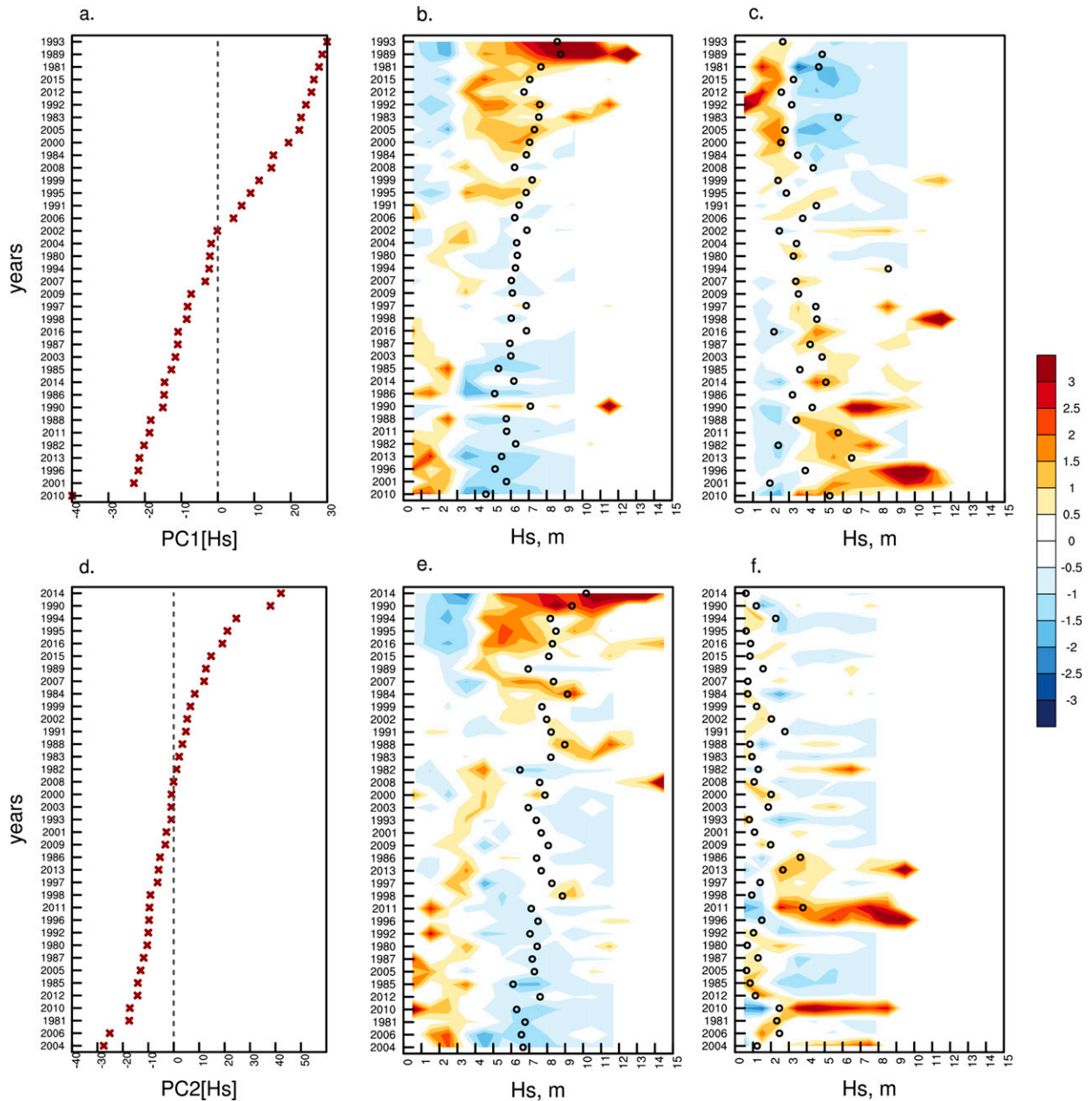


FIG. 11. Normalized occurrence anomalies of DJF H_s at locations where H_s variability is maximal in the (b),(c) first and (e),(f) second CCA modes for $[EKE_{LF}$ and $H_s]$. Locations are $2^\circ \times 2^\circ$ boxes centered on markers in Figs. 10c and 10d and labeled there by corresponding subplots in this figure. (a),(d) Years are ranked according to the first two principal components, respectively. Black circles show values for the 95th percentile of H_s .

and LF , respectively. The corresponding effective $C_D \times 10^3$ values are, therefore, 1.0 (*FULL*), 0.9 (*SUBS*), 0.7 (*SYNOB*), and 0.8 (*LF*) (Edson et al. 2013). Further examination of this issue is beyond the scope of this study since here we focus on the atmospheric dynamical controls of wave climate rather than the absolute veracity in the representation of air–sea interaction itself. All potential uncertainties and issues discussed above do not

limit the effectiveness of the conclusions we draw given the nature of this study.

Here, we have analyzed the large-scale atmospheric flow configurations driving wave climate responses. We do not account for the decomposition into wind sea and swell separately. Gulev and Grigorieva (2006) found that wind sea demonstrates the strongest association with the local wind speed, while swell is most sensitive to

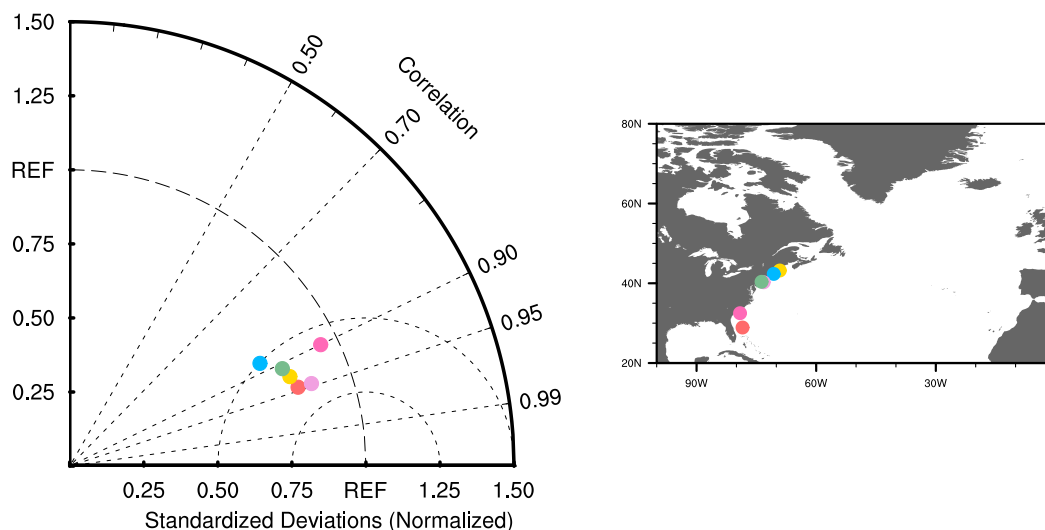


FIG. A1. Taylor diagram for H_s in reference model simulation (*FULL*) in comparison to NDBC buoys in DJF 2010.

the variation in cyclone frequency. In this way, the analysis of the interannual variability in wave climate and the identified remote responses in the near-coastal areas require consideration, specifically in the context of potentially different signals of these characteristics.

The analysis concept presented here provides an interesting avenue for the study of diversity in wind wave climate projections (e.g., Hemer et al. 2013; Fan et al. 2014; Wang et al. 2014; Aarnes et al. 2017). The NAO is projected to tend toward its positive phase in the upcoming century (e.g., Fan et al. 2013), which may be partially linked to high-confidence Arctic sea ice loss projections (Screen 2017). Thus, the local storm track and eddy-driven jet will likely experience corresponding perturbations (Ulbrich et al. 2013; Zappa et al. 2013b). We note this here since synoptic-scale atmospheric processes have been shown to play an important role in the distribution of mean and extreme waves, particularly along the North American coast.

A considerable question remains of how well global climate models from phase 5 of the Coupled Model Intercomparison Project (CMIP5) represent the behavior of individual atmospheric transient eddies. For example, the majority of global climate models demonstrate a reasonable number of extratropical cyclones; however, in most of them, the storm track is found to be either too zonally oriented or displaced southward in the central North Atlantic (Zappa et al. 2013a). CMIP5 global climate models also tend to underestimate cyclone intensity, specifically in the winter season (e.g., Zappa et al. 2013a). The magnitude of changes in storm track intensity in the Northern Hemisphere is the largest in the eastern North Atlantic and exceeds half of the interannual variability. This

result is found in up to 40% of CMIP5 models (Harvey et al. 2012) but, again, there is no consensus between models for areas with maximum H_s to the south of Iceland. This spread in uncertainties, which are all of atmospheric origin, resoundingly influences projections of wave climate, particularly in storm track influenced areas, such as the North Atlantic (Hemer et al. 2013). In this way, understanding the differential effect of atmospheric flow decomposed into different length scales on ocean surface waves can contribute a new perspective in understanding projections of future wind wave climate.

Ocean surface waves have been demonstrated to contribute to extreme water level events in coastal areas (Vitousek et al. 2017; Rueda et al. 2017; Vousedoukas et al. 2018; Melet et al. 2018). These works note specifically that the contributions of surface waves to sea level rise and associated events are both largely unconstrained and, for the most part, poorly appreciated. Given this, it is particularly relevant to observe regional responses of wave climate to variability in extratropical storm track activity.

6. Conclusions

We analyzed the different responses of the ocean surface wind wave field in the North Atlantic to atmospheric dynamical processes of various scales in boreal winter. For this purpose, we performed a suite of numerical experiments conducted with a spectral wave model forced by bandpass filtered winds. We, thus, decomposed atmospheric forcings into subsynoptic (<2 days), synoptic (2–10 days), and low-frequency (>10 days) components and specifically resolved the responses of wave climate to each of these individually.

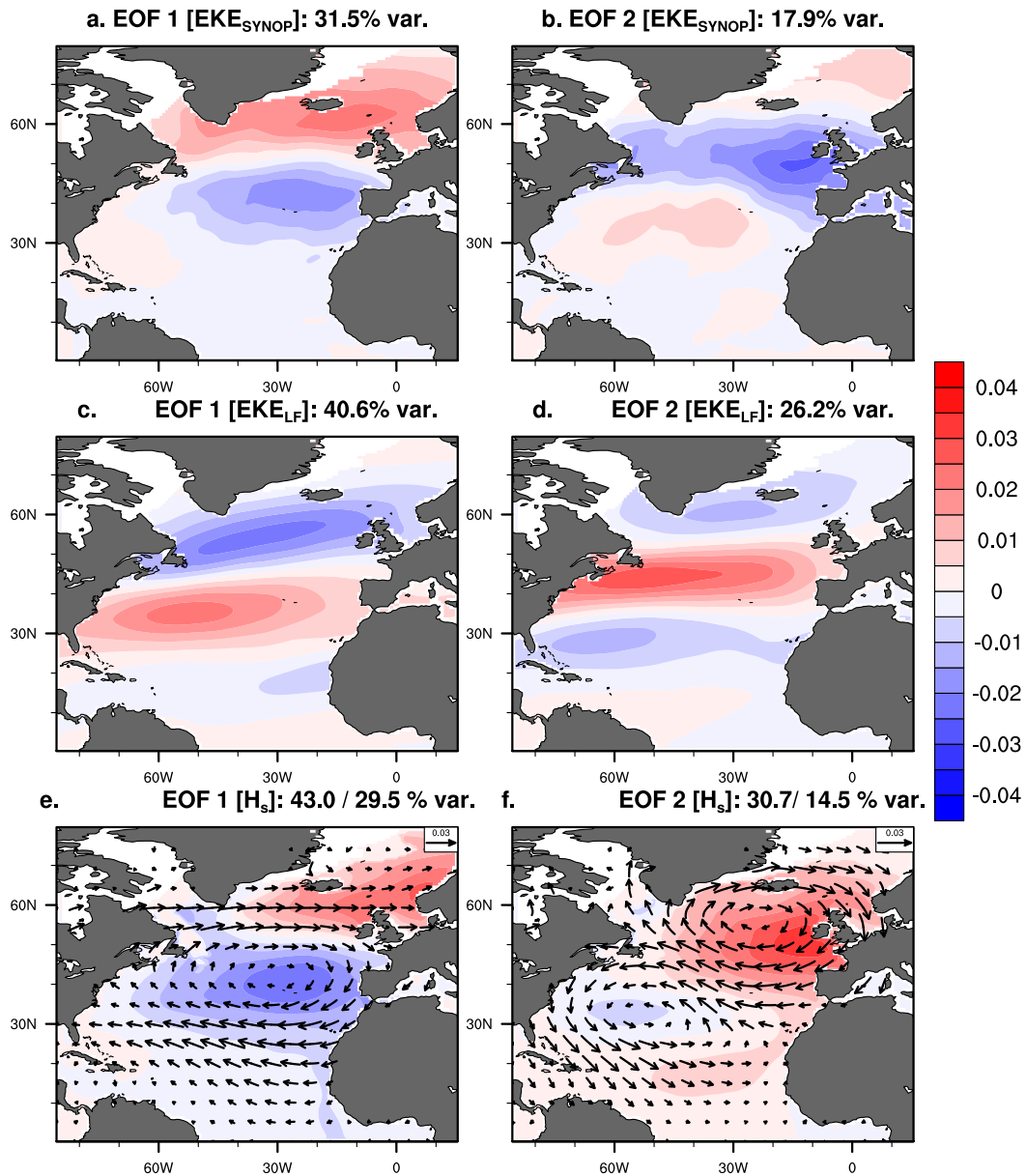


FIG. B1. Spatial distribution of first leading EOFs of seasonal mean storm track (defined as bandpass-filtered vertically integrated EKE) for (a),(b) synoptic variability of EKE (2–10 days), (c),(d) low-frequency variability of EKE (>10 days), and (e),(f) significant wave height and mean wave direction.

The region of the seasonal-maximum wave height in the North Atlantic is displaced northeastward of the area with the most vigorous tropospheric flow (measured here by vertically integrated EKE). The subsynoptic and synoptic-scale atmospheric forcings are found to have the largest impacts upon wind waves along the North American coastline and in the Labrador Sea (up to 70% of the total H_s). Meanwhile, in the midlatitudes, where the mean wintertime H_s is ~ 4.7 m, waves are generated by simultaneous contributions from both atmospheric synoptic-scale variability (i.e., transient atmospheric

eddies) and lower-frequency atmospheric forcing, such as prevailing westerlies. Subsynoptic-scale variability does not significantly contribute to the seasonal-mean wind wave characteristics but does have a considerable impact on the seasonal-maximum wave heights. This result is particularly true along the North American coastline and over the Gulf Stream region.

In subsequent analysis of responses to interannual atmospheric variability, we have concentrated on the influences of synoptic-scale transient eddies and low-frequency flow since they are found to have the largest

effects on both the absolute wave heights and interannual variability. Wind waves in the eastern mid-latitudes of the North Atlantic are strongly influenced by low-frequency atmospheric forcing, with only a low estimated upper bound for the contribution from synoptic-scale variability ($\sim 30\%$). Synoptic-scale processes in the western Atlantic are critical for modulating wind wave variability in the eastern midlatitudes. In this way, the reduction in wave heights along the European coast is likely associated with situations when weakening cyclone activity is observed over the North American eastern seaboard and more intensive zonal flow is observed within the low-frequency mode. At the same time, the meridional displacement of atmospheric transient eddies and low-frequency flow is associated with corresponding wave height anomalies. This relationship is also found to be reflected in the occurrence of anomalies in significant wave height distributions at sites along the eastern North Atlantic boundary. The change in the wave regime, which is well captured by the leading PCs of H_s , reflects a change in the ocean surface wave distribution and corresponding variability in extreme waves.

Acknowledgments. We are grateful to the three anonymous reviewers for extremely useful comments, which helped very much to improve the manuscript. We thank Cheikh Mbengue for the useful discussion, particularly regarding the Eulerian characterization of a storm track. We thank Kevin Hodges for providing the data on cyclone trajectories and very much appreciate his comments on the first versions of the manuscript. We thank Yulia Zyulyaeva for her methodological insights. We also thank Alexander Babanin and Bernard Barnier for more general discussions on the first manuscript versions. This work is the IORAS contribution to the ST-ASS-0149-2018-0001. This work was funded by Grant 17-77-20112 from the Russian Science Foundation (cyclone activity analysis) and Agreement 14.W0331.006 with the Ministry of Education and Science (analysis of forcing fields). WAVEWATCH III is available courtesy of the National Oceanic and Atmospheric Administration (NOAA). We thank the ECMWF for releasing their data to the public. These model experiments were conducted using the Lomonosov super-computer at Moscow State University.

APPENDIX A

Validation of Reference Simulations

The main body of the paper claims a good agreement between the model results and the ERA-Interim reanalysis (section 2a) and mentions that the model configuration

has been widely used in wave climate studies. However, as discussed above, coastal areas are particularly difficult to model with high accuracy, and models are known to underestimate higher-magnitude waves in particular (Stopa and Cheung 2014). Figure A1 shows the validation against buoy data from the National Data Buoy Center (NDBC; <http://www.ndbc.noaa.gov/>) along the U.S. eastern seaboard and demonstrates a mean Pearson correlation coefficient of 0.92 (varying from 0.9 to 0.95). In view of the arguments presented above, model results are considered to be reliable for the analysis conducted in this study.

APPENDIX B

EKE and Significant Wave Height EOFs

Figure B1 shows the EOFs for the seasonal-mean EKE_{SYNOPT} and EKE_{LF} , H_s , and θ . The synoptic and low-frequency modes of the EKE reveal similar patterns with H_s , with a significant portion of the total variance being contained within the first two EOFs. The first mode contains 40.6% and 31.5% of the variability in EKE_{LF} and EKE_{SYNOPT} , respectively, and 43% of the variability in significant wave height. The second EOF corresponds to 26.2% and 17.9% of the variability in EKE_{LF} and EKE_{SYNOPT} , respectively, and 30.7% of the variability in H_s , with smaller values for the subsequent modes. Regarding wave direction, the first EOF accounts for 29.5% and the second EOF accounts for 14.5% of the variability in θ . The correlation coefficient between the first PCs of H_s and EKE is 0.78 for the EKE synoptic mode and 0.92 for the EKE low-frequency mode (p value < 0.00001 in both cases), which confirms the link between these two characteristics.

REFERENCES

- Aarnes, O. J., and Coauthors, 2017: Projected changes in significant wave height toward the end of the 21st century: Northeast Atlantic. *J. Geophys. Res. Oceans*, **122**, 3394–3403, <https://doi.org/10.1002/2016JC012521>.
- Aijaz, S., M. Ghantous, A. V. Babanin, I. Ginis, B. Thomas, and G. Wake, 2017: Nonbreaking wave-induced mixing in upper ocean during tropical cyclones using coupled hurricane–ocean–wave modeling. *J. Geophys. Res. Oceans*, **122**, 3939–3963, <https://doi.org/10.1002/2016JC012219>.
- Alves, J.-H. G. M., 2006: Numerical modeling of ocean swell contributions to the global wind-wave climate. *Ocean Modell.*, **11**, 98–122, <https://doi.org/10.1016/j.ocemod.2004.11.007>.
- Andreas, E. L., L. Mahrt, and D. Vickers, 2015: An improved bulk air-sea flux algorithm, including spray-mediated transfer. *Quart. J. Roy. Meteor. Soc.*, **141**, 642–654, <https://doi.org/10.1002/qj.2424>.
- Ardhuin, F., B. Chapron, and F. Collard, 2009: Observation of swell dissipation across oceans. *Geophys. Res. Lett.*, **36**, L06607, <https://doi.org/10.1029/2008GL037030>.

- , and Coauthors, 2010: Semiempirical dissipation source functions for ocean waves. Part I: Definition, calibration, and validation. *J. Phys. Oceanogr.*, **40**, 1917–1941, <https://doi.org/10.1175/2010JPO4324.1>.
- Ayrault, F., F. Lalaurette, A. Joly, and C. Loo, 1995: North Atlantic ultra high frequency variability. *Tellus*, **47A**, 671–696, <https://doi.org/10.3402/tellusa.v47i5.11565>.
- Babanin, A. V., 2006: On a wave-induced turbulence and a wave-mixed upper ocean layer. *Geophys. Res. Lett.*, **33**, L20605, <https://doi.org/10.1029/2006GL027308>.
- , 2011: *Breaking and Dissipation of Ocean Surface Waves*. Cambridge University Press, 480 pp.
- , A. Ganopolski, and W. R. C. Phillips, 2009: Wave-induced upper-ocean mixing in a climate model of intermediate complexity. *Ocean Modell.*, **29**, 189–197, <https://doi.org/10.1016/j.ocemod.2009.04.003>.
- , M. Onorato, and F. Qiao, 2012: Surface waves and wave-coupled effects in lower atmosphere and upper ocean. *J. Geophys. Res.*, **117**, C00J01, <https://doi.org/10.1029/2012JC007932>.
- Bacon, S., and D. J. T. Carter, 1993: A connection between mean wave height and atmospheric pressure gradient in the North Atlantic. *Int. J. Climatol.*, **13**, 423–436, <https://doi.org/10.1002/joc.3370130406>.
- Bender, F., V. Ramanathan, and G. Tselioudis, 2012: Changes in extratropical storm track cloudiness 1983–2008: Observational support for a poleward shift. *Climate Dyn.*, **38**, 2037–2053, <https://doi.org/10.1007/s00382-011-1065-6>.
- Bender, M. A., T. R. Knutson, R. E. Tuleya, J. J. Sirutis, G. A. Vecchi, S. T. Garner, and I. M. Held, 2010: Modeled impact of anthropogenic warming on the frequency of intense Atlantic hurricanes. *Science*, **327**, 454–458, <https://doi.org/10.1126/science.1180568>.
- Bengtsson, L., K. Hodges, and E. Roeckner, 2006: Storm tracks and climate change. *J. Climate*, **19**, 3518–3543, <https://doi.org/10.1175/JCLI3815.1>.
- Blackmon, M., 1976: A climatological spectral study of the 500 mb geopotential height of the Northern Hemisphere. *J. Atmos. Sci.*, **33**, 1607–1623, [https://doi.org/10.1175/1520-0469\(1976\)033<1607:ACSSOT>2.0.CO;2](https://doi.org/10.1175/1520-0469(1976)033<1607:ACSSOT>2.0.CO;2).
- , J. Wallace, N.-C. Lau, and S. Mullen, 1977: An observational study of the Northern Hemisphere wintertime circulation. *J. Atmos. Sci.*, **34**, 1040–1053, [https://doi.org/10.1175/1520-0469\(1977\)034<1040:AOSOTN>2.0.CO;2](https://doi.org/10.1175/1520-0469(1977)034<1040:AOSOTN>2.0.CO;2).
- Booth, J. F., Y. Kwon, S. Ko, R. J. Small, and R. Msadek, 2017: Spatial patterns and intensity of the surface storm tracks in CMIP5 Models. *J. Climate*, **30**, 4965–4981, <https://doi.org/10.1175/JCLI-D-16-0228.1>.
- Caires, S., and A. Sterl, 2005: 100-year return value estimates for ocean wind speed and significant wave height from the ERA-40 data. *J. Climate*, **18**, 1032–1048, <https://doi.org/10.1175/JCLI-3312.1>.
- Camus, P., and Coauthors, 2014: A weather-type statistical downscaling framework for ocean wave climate. *J. Geophys. Res. Oceans*, **119**, 7389–7405, <https://doi.org/10.1002/2014JC010141>.
- Cardone, V. J., B. T. Callahan, H. Chen, A. T. Cox, M. A. Morrone, and V. R. Swail, 2015: Global distribution and risk to shipping of very extreme sea states (VESS). *Int. J. Climatol.*, **35**, 69–84, <https://doi.org/10.1002/joc.3963>.
- Carretero, J. C., and Coauthors, 1998: Changing waves and storms in the northeast Atlantic. *Bull. Amer. Meteor. Soc.*, **79**, 741–760, [https://doi.org/10.1175/1520-0477\(1998\)079<0741:CWASIT>2.0.CO;2](https://doi.org/10.1175/1520-0477(1998)079<0741:CWASIT>2.0.CO;2).
- Casas-Prat, M., X. L. Wang, and N. Swart, 2018: CMIP5-based global wave climate projections including the entire Arctic Ocean. *Ocean Modell.*, **123**, 66–85, <https://doi.org/10.1016/j.ocemod.2017.12.003>.
- Cavaleri, L., 2009: Wave modeling—Missing the peaks. *J. Phys. Oceanogr.*, **39**, 2757–2778, <https://doi.org/10.1175/2009JPO4067.1>.
- , and P. Malanotte-Rizzoli, 1981: Wind-wave prediction in shallow water: Theory and applications. *J. Geophys. Res.*, **86**, 10 961–10 973, <https://doi.org/10.1029/JC086iC11p10961>.
- , B. Fox-Kemper, and M. Hemer, 2012: Wind waves in the coupled climate system. *Bull. Amer. Meteor. Soc.*, **93**, 1651–1661, <https://doi.org/10.1175/BAMS-D-11-00170.1>.
- Chang, E. K. M., S. Lee, and K. L. Swanson, 2002: Storm track dynamics. *J. Climate*, **15**, 2163–2183, [https://doi.org/10.1175/1520-0442\(2002\)015<2021:STD>2.0.CO;2](https://doi.org/10.1175/1520-0442(2002)015<2021:STD>2.0.CO;2).
- Chawla, A., D. M. Spindler, and H. L. Tolman, 2013: Validation of a thirty year wave hindcast using the Climate Forecast System Reanalysis winds. *Ocean Modell.*, **70**, 189–206, <https://doi.org/10.1016/j.ocemod.2012.07.005>.
- Chen, G., B. Chapron, and R. Ezraty, 2002: A global view of swell and wind sea climate in the ocean by satellite altimeter and scatterometer. *J. Atmos. Oceanic Technol.*, **19**, 1849–1859, [https://doi.org/10.1175/1520-0426\(2002\)019<1849:AGVOSA>2.0.CO;2](https://doi.org/10.1175/1520-0426(2002)019<1849:AGVOSA>2.0.CO;2).
- D’Asaro, E., 2014: Turbulence in the upper-ocean mixed layer. *Annu. Rev. Mar. Sci.*, **6**, 101–115, <https://doi.org/10.1146/annurev-marine-010213-135138>.
- Dee, D. P., and Coauthors, 2011: The ERA-Interim reanalysis: Configuration and performance of the data assimilation system. *Quart. J. Roy. Meteor. Soc.*, **137**, 553–597, <https://doi.org/10.1002/qj.828>.
- de Leeuw, G., E. L. Andreas, M. D. Anguelova, C. W. Fairall, E. R. Lewis, C. O’Dowd, M. Schulz, and S. S. Schwartz, 2011: Production flux of sea spray aerosol. *Rev. Geophys.*, **49**, RG2001, <https://doi.org/10.1029/2010RG000349>.
- Delpey, M. T., F. Ardhuin, F. Collard, and B. Chapron, 2010: Space-time structure of long ocean swell fields. *J. Geophys. Res.*, **115**, C12037, <https://doi.org/10.1029/2009JC005885>.
- Duchon, C. E., 1979: Lanczos filtering in one and two dimensions. *J. Appl. Meteor.*, **18**, 1016–1022, [https://doi.org/10.1175/1520-0450\(1979\)018<1016:LFIOAT>2.0.CO;2](https://doi.org/10.1175/1520-0450(1979)018<1016:LFIOAT>2.0.CO;2).
- Edson, J. B., and Coauthors, 2013: On the exchange of momentum over the open ocean. *J. Phys. Oceanogr.*, **43**, 1589–1610, <https://doi.org/10.1175/JPO-D-12-0173.1>.
- Fan, Y., and S. Griffies, 2014: Impacts of parameterized Langmuir turbulence and nonbreaking wave mixing in global climate simulations. *J. Climate*, **27**, 4752–4775, <https://doi.org/10.1175/JCLI-D-13-00583.1>.
- , I. Ginis, and T. Hara, 2009: The effect of wind–wave–current interaction on air–sea momentum fluxes and ocean response in tropical cyclones. *J. Phys. Oceanogr.*, **39**, 1019–1034, <https://doi.org/10.1175/2008JPO4066.1>.
- , I. M. Held, S.-J. Lin, and X. L. Wang, 2013: Ocean warming effect on surface gravity wave climate change for the end of the twenty-first century. *J. Climate*, **26**, 6046–6066, <https://doi.org/10.1175/JCLI-D-12-00410.1>.
- , S.-J. Lin, S. M. Griffies, and M. A. Hemer, 2014: Simulated global swell and wind-sea climate and their responses to anthropogenic climate change at the end of the twenty-first century. *J. Climate*, **27**, 3516–3536, <https://doi.org/10.1175/JCLI-D-13-00198.1>.
- Foussard, A., G. Lapeyre, and R. Plougonven, 2019: Storm tracks response to oceanic eddies in idealized atmospheric simulations. *J. Climate*, **32**, 445–463, <https://doi.org/10.1175/JCLI-D-18-0415.1>.
- Gulev, S. K., and L. Hasse, 1998: North Atlantic wind waves and wind stress from voluntary observing ship data. *J. Phys. Oceanogr.*,

- 28, 1107–1130, [https://doi.org/10.1175/1520-0485\(1998\)028<1107:NAWWAW>2.0.CO;2](https://doi.org/10.1175/1520-0485(1998)028<1107:NAWWAW>2.0.CO;2).
- , and —, 1999: Changes of wind waves in the North Atlantic over the last 30 years. *Int. J. Climatol.*, **19**, 1091–1117, [https://doi.org/10.1002/\(SICI\)1097-0088\(199908\)19:10<1091::AID-JOC403>3.0.CO;2-U](https://doi.org/10.1002/(SICI)1097-0088(199908)19:10<1091::AID-JOC403>3.0.CO;2-U).
- , and V. Grigorieva, 2006: Variability of winter wind waves and swell in the North Atlantic and North Pacific as revealed by the voluntary observing ship data. *J. Climate*, **19**, 5667–5685, <https://doi.org/10.1175/JCLI3936.1>.
- , T. Jung, and E. Ruprecht, 2002: Climatology and interannual variability in the intensity of synoptic-scale processes in the North Atlantic from the NCEP–NCAR reanalysis data. *J. Climate*, **15**, 809–828, [https://doi.org/10.1175/1520-0442\(2002\)015<0809:CAIVIT>2.0.CO;2](https://doi.org/10.1175/1520-0442(2002)015<0809:CAIVIT>2.0.CO;2).
- , V. Grigorieva, A. Sterl, and D. Woolf, 2003: Assessment for the reliability of wave observations from voluntary observing ships: Insights from the validation of a global wind wave climatology based on voluntary observing ship data. *J. Geophys. Res.*, **108**, 3236, <https://doi.org/10.1029/2002JC001437>.
- Hanley, K. E., S. E. Belcher, and P. R. Sullivan, 2010: A global climatology of wind–wave interaction. *J. Phys. Oceanogr.*, **40**, 1263–1282, <https://doi.org/10.1175/2010JPO4377.1>.
- Harvey, B. J., L. C. Shaffrey, T. J. Woollings, G. Zappa, and K. I. Hodges, 2012: How large are projected 21st century storm track changes? *Geophys. Res. Lett.*, **39**, L18707, <https://doi.org/10.1029/2012GL052873>.
- Hasselmann, S., and K. Hasselmann, 1985: Computations and parameterizations of the nonlinear energy transfer in a gravity-wave spectrum. Part I: A new method for efficient computations of the exact nonlinear transfer integral. *J. Phys. Oceanogr.*, **15**, 1369–1377, [https://doi.org/10.1175/1520-0485\(1985\)015<1369:CAPOTN>2.0.CO;2](https://doi.org/10.1175/1520-0485(1985)015<1369:CAPOTN>2.0.CO;2).
- Held, I. M., and B. J. Hoskins, 1985: Large-scale eddies and the general circulation of the troposphere. *Advances in Geophysics*, Vol. 28, Academic Press, 3–31, [https://doi.org/10.1016/S0065-2687\(08\)60218-6](https://doi.org/10.1016/S0065-2687(08)60218-6).
- Hemer, M. A., Y. Fan, N. Mori, A. Semedo, and X. L. Wang, 2013: Projected changes in wave climate from a multi-model ensemble. *Nat. Climate Change*, **3**, 471–476, <https://doi.org/10.1038/nclimate1791>.
- Hodges, K. I., 1995: Feature tracking on the unit sphere. *Mon. Wea. Rev.*, **123**, 3458–3465, [https://doi.org/10.1175/1520-0493\(1995\)123<3458:FTOTUS>2.0.CO;2](https://doi.org/10.1175/1520-0493(1995)123<3458:FTOTUS>2.0.CO;2).
- Högström, U., A. Smedman, E. Sahlé, W. M. Drennan, K. K. Kahma, H. Pettersson, and F. Zhang, 2009: The atmospheric boundary layer during swell: A field study and interpretation of the turbulent kinetic energy budget for high wave ages. *J. Atmos. Sci.*, **66**, 2764–2779, <https://doi.org/10.1175/2009JAS2973.1>.
- Hoskins, B., and K. Hodges, 2002: New perspectives on the Northern Hemisphere winter storm tracks. *J. Atmos. Sci.*, **59**, 1041–1061, [https://doi.org/10.1175/1520-0469\(2002\)059<1041:NPOTNH>2.0.CO;2](https://doi.org/10.1175/1520-0469(2002)059<1041:NPOTNH>2.0.CO;2).
- Janssen, P. A. E. M., 2015: Notes on the maximum wave height distribution. ECMWF Tech. Memo. 755, 21 pp.
- Jiménez, P. A., J. Dudhia, J. F. González-Rouco, J. Navarro, J. P. Montávez, and E. García-Bustamante, 2012: A revised scheme for the WRF surface layer formulation. *Mon. Wea. Rev.*, **140**, 898–918, <https://doi.org/10.1175/MWR-D-11-00056.1>.
- Khon, V. C., I. I. Mokhov, F. A. Pogarskiy, A. Babanin, K. Dethloff, A. Rinke, and H. Matthes, 2014: Wave heights in the 21st century Arctic Ocean simulated with a regional climate model. *Geophys. Res. Lett.*, **41**, 2956–2961, <https://doi.org/10.1002/2014GL059847>.
- Knutson, T. R., and Coauthors, 2013: Dynamical downscaling projections of twenty-first-century Atlantic hurricane activity: CMIP3 and CMIP5 model-based scenarios. *J. Climate*, **26**, 6591–6617, <https://doi.org/10.1175/JCLI-D-12-00539.1>.
- Kohout, A. L., M. J. M. Williams, S. M. Dean, and M. H. Meylan, 2014: Storm-induced sea-ice breakup and the implications for ice extent. *Nature*, **509**, 604–607, <https://doi.org/10.1038/nature13262>.
- Komen, G. J., L. Cavaleri, M. Donelan, K. Hasselmann, S. Hasselmann, and P. A. E. M. Janssen, 1994: *Dynamics and Modelling of Ocean Waves*. Cambridge University Press, 532 pp.
- Lanczos, C., 1956: *Applied Analysis*. Prentice-Hall, 539 pp.
- Lorenz, D. J., and E. T. DeWeaver, 2007: Tropopause height and zonal wind response to global warming in the IPCC scenario integrations. *J. Geophys. Res.*, **112**, D10119, <https://doi.org/10.1029/2006JD008087>.
- Lorenz, E. N., 1955: Available potential energy and the maintenance of the general circulation. *Tellus*, **7**, 157–167, <https://doi.org/10.3402/tellusa.v7i2.8796>.
- Lozano, I., and V. Swail, 2002: The link between wave height variability in the North Atlantic and the storm track activity in the last four decades. *Atmos.–Ocean*, **40**, 377–388, <https://doi.org/10.3137/ao.400401>.
- Markina, M., A. Gavrikov, S. Gulev, and B. Barnier, 2018: Developing configuration of WRF model for long-term high-resolution wind wave hindcast over the North Atlantic with WAVEWATCH III. *Ocean Dyn.*, **68**, 1593–1604, <https://doi.org/10.1007/s10236-018-1215-z>.
- Martínez-Asensio, A., M. N. Tsimplis, M. Marcos, X. Feng, D. Gomis, G. Jordà, and S. A. Josey, 2016: Response of the North Atlantic wave climate to atmospheric modes of variability. *Int. J. Climatol.*, **36**, 1210–1225, <https://doi.org/10.1002/joc.4415>.
- Massom, R. A., T. A. Scambos, L. G. Bennets, P. Reid, V. A. Squire, and S. E. Stammerjohn, 2018: Antarctic ice shelf disintegration triggered by sea ice loss and ocean swell. *Nature*, **558**, 383–389, <https://doi.org/10.1038/s41586-018-0212-1>.
- Mbengue, C., and T. Schneider, 2013: Storm track shifts under climate change: What can be learned from large-scale dry dynamics. *J. Climate*, **26**, 9923–9930, <https://doi.org/10.1175/JCLI-D-13-00404.1>.
- , and —, 2017: Storm-track shifts under climate change: Toward a mechanistic understanding using baroclinic mean available potential energy. *J. Atmos. Sci.*, **74**, 93–110, <https://doi.org/10.1175/JAS-D-15-0267.1>.
- , T. Woollings, H. F. Dacre, and K. I. Hodges, 2018: The roles of static stability and tropical–extratropical interactions in the summer interannual variability of the North Atlantic sector. *Climate Dyn.*, <https://doi.org/10.1007/s00382-018-4192-5>.
- Melet, A., B. Meyssignac, R. Almar, and G. Le Cozannet, 2018: Under-estimated wave contribution to coastal sea-level rise. *Nat. Climate Change*, **8**, 234–239, <https://doi.org/10.1038/s41558-018-0088-y>.
- Miles, J. M., 1957: On the generation of surface waves by shear flows. *J. Fluid Mech.*, **3**, 185–204, <https://doi.org/10.1017/S0022112057000567>.
- Monin, A. S., and A. M. Obukhov, 1954: Basic laws of turbulent mixing in the atmosphere near the ground. *Tr. Inst. Teor. Geofiz. Akad. Nauk SSSR*, **24**, 1963–1987.
- Neu, U., and Coauthors, 2013: IMILAST: A community effort to intercompare extratropical cyclone detection and tracking algorithms. *Bull. Amer. Meteor. Soc.*, **94**, 529–547, <https://doi.org/10.1175/BAMS-D-11-00154.1>.
- Obukhov, A. M., 1946: Turbulence in thermally non-homogeneous atmosphere. *Tr. Inst. Teor. Geofiz. Akad. Nauk SSSR*, **1**, 95–115.

- Orlanski, I., and J. Katzfey, 1991: The life cycle of a cyclone wave in the Southern Hemisphere. Part I: Eddy energy budget. *J. Atmos. Sci.*, **48**, 1972–1998, [https://doi.org/10.1175/1520-0469\(1991\)048<1972:TLCOAC>2.0.CO;2](https://doi.org/10.1175/1520-0469(1991)048<1972:TLCOAC>2.0.CO;2).
- Phibbs, S., and R. Toumi, 2014: Modeled dependence of wind and waves on ocean temperature in tropical cyclones. *Geophys. Res. Lett.*, **41**, 7383–7390, <https://doi.org/10.1002/2014GL061721>.
- Pinto, J. G., U. Ulbrich, G. C. Leckebusch, T. Spanghel, M. Meyers, and S. Zacharias, 2007: Changes in storm track and cyclone activity in three SRES ensemble experiments with the ECHAM5/MPI-OM1 GCM. *Climate Dyn.*, **29**, 195–210, <https://doi.org/10.1007/s00382-007-0230-4>.
- Qiao, F., Y. Yuan, J. Deng, D. Dai, and Z. Song, 2016: Wave–turbulence interaction-induced vertical mixing and its effects in ocean and climate models. *Philos. Trans. Roy. Soc.*, **375A**, 20150201, <https://doi.org/10.1098/rsta.2015.0201>.
- Rasche, N., and F. Ardhuin, 2013: A global wave parameter database for geophysical applications. Part 2: Model validation with improved source term parameterization. *Ocean Modell.*, **70**, 174–188, <https://doi.org/10.1016/j.ocemod.2012.12.001>.
- Roberts, J. F., and Coauthors, 2014: The XWS open access catalogue of extreme European windstorms from 1979 to 2012. *Nat. Hazards Earth Syst. Sci.*, **14**, 2487–2501, <https://doi.org/10.5194/nhess-14-2487-2014>.
- Rudeva, I., and S. K. Gulev, 2011: Composite analysis of the North Atlantic extratropical cyclones in NCEP/NCAR reanalysis. *Mon. Wea. Rev.*, **139**, 1419–1446, <https://doi.org/10.1175/2010MWR3294.1>.
- Rueda, A., and Coauthors, 2017: A global classification of coastal flood hazard climates associated with large-scale oceanographic forcing. *Sci. Rep.*, **7**, 5038, <https://doi.org/10.1038/s41598-017-05090-w>.
- Schneider, T., T. Bischoff, and H. Plotka, 2015: Physics of changes in synoptic midlatitude temperature variability. *J. Climate*, **28**, 2312–2331, <https://doi.org/10.1175/JCLI-D-14-00632.1>.
- Screen, J. A., 2017: Simulated atmospheric response to regional and pan-Arctic sea ice loss. *J. Climate*, **30**, 3945–3962, <https://doi.org/10.1175/JCLI-D-16-0197.1>.
- Semedo, A., K. Sušelj, and A. Rutgersson, 2008: Variability of wind sea and swell waves in the North Atlantic based on ERA-40 reanalysis. *Proc. Eighth European Wave and Tidal Energy Conf.*, Uppsala, Sweden, EWTEC, 119–129.
- , —, —, and A. Sterl, 2011: A global view on the wind sea and swell climate and variability from ERA-40. *J. Climate*, **24**, 1461–1479, <https://doi.org/10.1175/2010JCLI3718.1>.
- , R. Vettor, Ø. Breivik, A. Sterl, M. Reistad, C. G. Soares, and D. Lima, 2015: The wind sea and swell waves climate in the Nordic seas. *Ocean Dyn.*, **65**, 223–240, <https://doi.org/10.1007/s10236-014-0788-4>.
- Snodgrass, F. E., G. W. Groves, K. F. Hasselmann, G. R. Miller, W. H. Munk, and W. M. Powers, 1966: Propagation of ocean swell across the Pacific. *Philos. Trans. Roy. Soc. London*, **259A**, 431–497, <https://doi.org/10.1098/rsta.1966.0022>.
- Stoll, P. J., R. G. Graversen, G. Noer, and K. Hodges, 2018: An objective global climatology of polar lows based on reanalysis data. *Quart. J. Roy. Meteor. Soc.*, **144**, 2099–2117, <https://doi.org/10.1002/qj.3309>.
- Stoney, L., K. J. E. Walsh, S. Thomas, P. Spence, and A. V. Babanin, 2018: Changes in ocean heat content caused by wave-induced mixing in a high-resolution ocean model. *J. Phys. Oceanogr.*, **48**, 1139–1150, <https://doi.org/10.1175/JPO-D-17-0142.1>.
- Stopa, J. E., and K. F. Cheung, 2014: Intercomparison of wind and wave data from the ECMWF Reanalysis Interim and the NCEP Climate Forecast System Reanalysis. *Ocean Modell.*, **75**, 65–83, <https://doi.org/10.1016/j.ocemod.2013.12.006>.
- Studholme, J. H. P., and S. K. Gulev, 2018: Concurrent changes to Hadley circulation and the meridional distribution of tropical cyclones. *J. Climate*, **31**, 4367–4389, <https://doi.org/10.1175/JCLI-D-17-0852.1>.
- Sullivan, P. P., and J. C. McWilliams, 2002: Turbulent flow over water waves in the presence of stratification. *Phys. Fluids*, **14**, 1182–1195, <https://doi.org/10.1063/1.1447915>.
- Tamarin-Brodsky, T., and Y. Kaspi, 2017: Enhanced poleward propagation of storms under climate change. *Nat. Geosci.*, **10**, 908–913, <https://doi.org/10.1038/s41561-017-0001-8>.
- Teague, W. J., E. Jarosz, D. W. Wang, and D. A. Mitchell, 2007: Observed oceanic response over the upper continental slope and outer shelf during Hurricane Ivan. *J. Phys. Oceanogr.*, **37**, 2181–2206, <https://doi.org/10.1175/JPO3115.1>.
- Thomson, J., and W. E. Rogers, 2014: Swell and sea in the emerging Arctic Ocean. *Geophys. Res. Lett.*, **41**, 3136–3140, <https://doi.org/10.1002/2014GL059983>.
- Tilinina, N., S. K. Gulev, I. Rudeva, and P. Koltermann, 2013: Comparing cyclone life cycle characteristics and their interannual variability in different reanalyses. *J. Climate*, **26**, 6419–6438, <https://doi.org/10.1175/JCLI-D-12-00777.1>.
- Tolman, H. L., 2003: Treatment of unresolved islands and ice in wind wave models. *Ocean Modell.*, **5**, 219–231, [https://doi.org/10.1016/S1463-5003\(02\)00040-9](https://doi.org/10.1016/S1463-5003(02)00040-9).
- Ulbrich, U., J. G. Pinto, H. Kupfer, G. C. Leckebusch, T. Spanghel, and M. Meyers, 2008: Changing Northern Hemisphere storm tracks in an ensemble of IPCC climate change simulations. *J. Climate*, **21**, 1669–1679, <https://doi.org/10.1175/2007JCLI1992.1>.
- , and Coauthors, 2013: Are greenhouse gas signals of Northern Hemisphere winter extra-tropical cyclone activity dependent on the identification and tracking algorithm? *Meteor. Z.*, **22**, 61–68, <https://doi.org/10.1127/0941-2948/2013/0420>.
- Våge, K., T. Spengler, H. C. Davies, and R. S. Pickart, 2009: Multi-event analysis of the westerly Greenland tip jet based upon 45 winters in ERA-40. *Quart. J. Roy. Meteor. Soc.*, **135**, 1999–2011, <https://doi.org/10.1002/qj.488>.
- Veron, F., W. K. Melville, and L. Lenain, 2008: Wave-coherent air–sea heat flux. *J. Phys. Oceanogr.*, **38**, 788–802, <https://doi.org/10.1175/2007JPO3682.1>.
- Vitousek, S., P. L. Barnard, C. H. Fletcher, N. Frazer, L. Erikson, and C. D. Storlazzi, 2017: Doubling of coastal flooding frequency within decades due to sea-level rise. *Sci. Rep.*, **7**, 1399, <https://doi.org/10.1038/s41598-017-01362-7>.
- von Storch, H., and F. W. Zwiers, 1999: *Statistical Analysis in Climate Research*. Cambridge University Press, 503 pp.
- Vousdoukas M. I., L. Mentaschi, E. Voukouvalas, M. Verlaan, S. Jevrejeva, L. P. Jackson, and L. Feyen, 2018: Global probabilistic projections of extreme sea levels show intensification of coastal flood hazard. *Nat. Commun.*, **9**, 2360, <https://doi.org/10.1038/s41467-018-04692-w>.
- Walsh, K., P. Govekar, A. V. Babanin, M. Ghantous, P. Spence, and E. Scoccimarro, 2017: The effect on simulated ocean climate of a parameterization of unbroken wave-induced mixing incorporated into the k-epsilon mixing scheme. *J. Adv. Model. Earth Syst.*, **9**, 735–758, <https://doi.org/10.1002/2016MS000707>.
- Wang, X. L., and V. R. Swail, 2001: Changes of extreme wave heights in Northern Hemisphere oceans and related atmospheric circulation regimes. *J. Climate*, **14**, 2204–2221, [https://doi.org/10.1175/1520-0442\(2001\)014<2204:COEWHI>2.0.CO;2](https://doi.org/10.1175/1520-0442(2001)014<2204:COEWHI>2.0.CO;2).

- , F. W. Zwiers, and V. R. Swail, 2004: North Atlantic Ocean wave climate change scenarios for the twenty-first century. *J. Climate*, **17**, 2368–2383, [https://doi.org/10.1175/1520-0442\(2004\)017<2368:NAOWCC>2.0.CO;2](https://doi.org/10.1175/1520-0442(2004)017<2368:NAOWCC>2.0.CO;2).
- , Y. Feng, and V. R. Swail, 2014: Changes in global ocean wave heights as projected using multimodel CMIP5 simulations. *Geophys. Res. Lett.*, **41**, 1026–1034, <https://doi.org/10.1002/2013GL058650>.
- Waseda, T., A. Webb, K. Sato, J. Inoue, A. Kohout, B. Penrose, and S. Penrose, 2018: Correlated increase of high ocean waves and winds in the ice-free waters of the Arctic Ocean. *Sci. Rep.*, **8**, 4489, <https://doi.org/10.1038/s41598-018-22500-9>.
- WAVEWATCH III Development Group, 2016: User manual and system documentation of WAVEWATCH III R version 5.16. NOAA/NWS/NCEP/MMAB Tech. Note 329, 326 pp. + appendices.
- Woolf, D., P. Challenor, and P. Cotton, 2002: Variability and predictability of the North Atlantic wave climate. *J. Geophys. Res.*, **107**, 3145, <https://doi.org/10.1029/2001JC001124>.
- Woollings, T., and M. Blackburn, 2012: The North Atlantic jet stream under climate change and its relation to the NAO and EA patterns. *J. Climate*, **25**, 886–902, <https://doi.org/10.1175/JCLI-D-11-00087.1>.
- , J. M. Gregory, J. G. Pinto, M. Reyers, and D. J. Brayshaw, 2012: Response of the North Atlantic storm track to climate change shaped by ocean–atmosphere coupling. *Nat. Geosci.*, **5**, 313–317, <https://doi.org/10.1038/ngeo1438>.
- , L. Papritz, C. Mbengue, and T. Spengler, 2016: Diabatic heating and jet stream shifts: A case study of the 2010 negative North Atlantic oscillation winter. *Geophys. Res. Lett.*, **43**, 9994–10002, <https://doi.org/10.1002/2016GL070146>.
- Yin, J. H., 2005: A consistent poleward shift of the storm track in simulations of 21st century climate. *Geophys. Res. Lett.*, **32**, L18701, <https://doi.org/10.1029/2005GL023684>.
- Young, I. R., S. Zieger, and A. V. Babanin, 2011: Global trends in wind speed and wave height. *Science*, **332**, 451–455, <https://doi.org/10.1126/science.1197219>.
- , E. Sanina, and A. V. Babanin, 2017: Calibration and cross validation of a global wind and wave database of altimeter, radiometer, and scatterometer measurements. *J. Atmos. Oceanic Technol.*, **34**, 1285–1306, <https://doi.org/10.1175/JTECH-D-16-0145.1>.
- Zappa, G., L. C. Shaffrey, and K. I. Hodges, 2013a: The ability of CMIP5 models to simulate North Atlantic extratropical cyclones. *J. Climate*, **26**, 5379–5396, <https://doi.org/10.1175/JCLI-D-12-00501.1>.
- , —, —, P. G. Sansom, and D. B. Stephenson, 2013b: A multimodel assessment of future projections of North Atlantic and European extratropical cyclones in the CMIP5 climate models. *J. Climate*, **26**, 5846–5862, <https://doi.org/10.1175/JCLI-D-12-00573.1>.
- Zieger, S., J. Vioth, and I. R. Young, 2009: Joint calibration of multiplatform altimeter measurements of wind speed and wave height over the past 20 years. *J. Atmos. Oceanic Technol.*, **26**, 2549–2564, <https://doi.org/10.1175/2009JTECHA1303.1>.